KINETICS OF FISSION PRODUCT RELEASE PRIOR TO FUEL SLUMPING*

by

J. Rest

Materials and Components Technology Division
ARGONNE NATIONAL LABORATORY
Argonne, Illinois   60439

October 1987

KINETICS OF FISSION PRODUCT RELEASE PRIOR TO FUEL SLUMPING*

by

J. Rest
Materials and Components Technology Division
ARGONNE NATIONAL LABORATORY
Argonne, Illinois 60439

ABSTRACT

This paper describes the primary physical/chemical models recently
incorporated into a mechanistic code (FASTGRASS) for the estimation of fission
product release from fuel, and compares predicted results with test data. The
theory of noble gas behavior is discussed in relation to its effect on the
release behavior of I, Cs, Te, Ba, and Sr. The behavior of these fission
products in the presence of fuel liquefaction/dissolution and oxidation grain-
growth phenomena is presented, as is the chemistry of Sr, Ba, I, and Cs.

Comparison of code predictions with data indicates the following
trends. Fission product release behavior from solid fuel strongly depends on
fuel microstructure, irradiation history, time at temperature, and internal
fuel rod chemistry. Fuel liquefaction/dissolution, fracturing, and oxidation
also exert a pronounced effect on release during fuel rod degradation.
For very low burnup fuel appreciable fission product retention in
previously liquefied fuel can occur due to the low concentration of fission
products, and the limited growth of bubbles in the liquefied material.

---

1.   Introduction

Both the Three Mile Island (TMI)-2 and Chernobyl accidents have increased public awareness of the potential for large-scale fission product release during severe core damage accidents. Both events resulted in significant release of noble gases (Xe, Kr), and volatile (I, Te, Cs) and alkaline earth (Sr, and Ba) radionuclides from the fuel itself. Although differences in primary coolant and containment building design largely determined the ultimate plant release characteristics, a detailed analysis of fission product release for severe accidents requires an adequate time-dependent prediction of volatile fission product (VFP), and alkaline earth fission product (AEFP) release from fuel, with subsequent analysis of the transport behavior of fission products from the degraded core, primary system, and containment. The first step in this analysis is the prediction of VFP and AEFP release behavior from severely damaged fuel. This paper describes the primary physical/chemical models recently incorporated into a mechanistic code, FASTGRASS, for the estimation of the release of six different fission products, including those with the most serious effects on human health. In terms of the health consequences, as indicated in Table 1, I, Te, and Cs are the primary risk-dominant radionuclides associated with the release of fission product during severe core accidents.[1] The next most important fission products with respect to the public health hazard are Sr, Ru, and Ba.

Section 2 of this paper presents an overview of the modeling of noble gas release from solid fuel, which plays a major role in establishing a route for fission product migration from the interior of the solid fuel matrix to the exterior or escape surface. Section 2 also describes the chemical interactions between reactive fission products (e.g., I, Cs, Ba, and Sr) and the fuel matrix. Section 3 describes phenomena affecting fission product

release under severe accident conditions, where fuel-oxidation-induced grain growth, molten-zircaloy-cladding-induced fuel dissolution/liquefaction, and quench-induced fuel shattering occur. Section 4 compares the theory and two data sets: (1) data from out-of-reactor induction heating experiments on declad low-burnup (1000 and 4000 MWd/t) pellets and (2) data from the more recent in-reactor Power Burst Facility (PBF) Severe Fuel Damage (SFD) Tests, in which one-meter-long, trace-irradiated (89 MWd/t) and normally irradiated (~34000 MWd/t) fuel rods were tested under accident conditions. Section 5 compares fission product release from normally irradiated fuel during out-of-reactor high-temperature heating tests in a flowing steam atmosphere using an NRC empirical model and FASTGRASS. Section 6 presents remarks and conclusions.

Table 1. Ranking of Radionuclides with Respect to Health Effects

Element	Rank	Ranking Factor[a]
Iodine, I	1	38
Tellurium, Te	2	37
Cesium, Cs	3	31
Strontium, Sr	(4)[b]	16
Ruthenium, Ru	(4)	16
Barium, Ba	6	11
Yttrium, Y	7	6
Cerium, Ce	(8)	5
Antimony, Sb	(8)	5
Plutonium, Pu	(10)	4
Curium, Cm	(10)	4
Molybdenum, Mo	(12)	3
Lanthanum, La	(12)	3

[a]Ranking factor based upon amount of species released and health consequences.
[b]Parentheses denote equivalence in rank.

2. FASTGRASS Theory of Fission Gas Behavior in Solid Fuel

The FASTGRASS code mechanistically predicts atomic and bubble behavior of fission gas in UO_2 fuel under steady-state and transient conditions. Models are included that assess the effects of fission product generation, atomic migration, bubble nucleation and re-solution, bubble migration and coalescence, channel formation on grain faces, interlinking on grain edges, and microcracking on both the amount of fission products released and on their distribution within the fuel. FASTGRASS solves a set of coupled nonlinear differential equations for the intra- and intergranular concentrations of fission product atoms and gas bubbles of the form

$$\frac{dC_i}{dt} = -a_i C_i^2 - b_i C_i + e_i. \tag{1}$$

The variables appearing in Eq. (1) are defined in Table 2, and have been discussed, for the most part, in previous papers.[2-4] However, for the sake of clarity, the basic equations solved in FASTGRASS are summarized below. In these basic equations, C_g, C_b, C_f and C_e are the concentrations of intragranular gas atoms, gas bubbles, grain face bubbles, and grain edge bubbles, respectively, and N_b, N_f, and N_e are the corresponding number of gas atoms per bubble.

Intragranular fission gas

The concentration of gas atoms, C_g, is determined by solving

Table 2. Definition of Variables in Eq. (1), $dC_i/dt = -a_i C_i^2 - b_i C_i + e_i$

C_i	$a_i C_i^2$	$b_i C_i$	e_i
Concentration of intragranular gas atoms, VFPs, and AEFPs	Rate at which gas atoms are lost owing to gas bubble nucleation	Rate at which gas atoms, VFPs, and AEFPs are lost owing to radiolytic decay, diffusive flow to the grain boundaries, grain boundary sweeping, diffusion into gas bubbles, chemical reactions, and fuel dissolution	Rate at which atoms VFPs and AEFPs are gained owing to atom re-solution, fission of uranium nuclei, chemical reactions, and long-range migration
Concentration of intragranular gas bubbles	Rate at which gas bubbles are lost owing to bubble coalescence	Rate at which gas bubbles are lost owing to diffusive flow to the grain boundaries, grain boundary sweeping, gas atom re-solution, and fuel dissolution	Rate at which gas bubbles are gained owing to bubble nucleation, diffusion of gas atoms into bubbles, and long-range migration
Concentration of grain face gas bubbles, VFPs, and AEFPs	Rate at which gas bubbles are lost owing to bubble coalescence	Rate at which gas bubbles, VFPs, and AEFPs are lost owing to diffusion to grain edges, formation of grain face channels, microcracking, chemical reactions, fuel liquefaction/dissolution, and long-range migration	Rate at which gas bubbles VFPs and AEFPs are gained owing to intragranular migration to grain faces, chemical reactions, and long-range migration
Concentration of grain edge gas bubbles, VFPs and AEFPs	Rate at which gas bubbles are lost owing to bubble coalescence	Rate at which gas bubbles, VFPs, and AEFPs are lost owing to long-range grain-edge bubble interconnection, microcracking, chemical reactions, and fuel liquefaction/dissolution	Rate at which gas bubbles VFPs and AEFPs are gained owing to migration of grain-face fission products to grain edges and chemical reactions

5

$$\frac{dC_g}{dt} = -16\pi F_N R_g D_g C_g^2 - 4\pi(D_g + D_b)(R_g + R_b)C_g C_b$$

$$- \pi|V_b - V_g|(R_g + R_b)^2 C_g C_b - S_v^{\alpha\alpha} V_g C_g$$

$$+ \frac{6D_g}{d_g}\left.\frac{\partial C_g}{\partial r}\right|_{r=d_g/2} - \pi C_g d_g^2(t)V_{gb}/2$$

$$+ \beta\dot{f} + bN_b C_b + \delta bN_f C_f + \delta bN_e C_e. \tag{2}$$

In Eq. (2), R_g, R_b and D_g, D_b and V_g, V_b are the radii of the intragranular gas atom and gas bubble, diffusion coefficients, and velocities, respectively. F_N is the nucleation factor, i.e., the probability that two gas atoms which have come together actually stick. $S_v^{\alpha\alpha}$ is the grain boundary area per unit volume; d_g, the grain diameter; $\dot{f}$, the fission rate (fissions/cc/s); and β, the number of gas atoms produced per fission. The successive terms on the right hand side (RHS) of Eq. (2) represent, respectively, 1, the loss of gas atoms due to bubble nucleation; 2 and 3, the random and biased capture of gas atoms by bubbles; 4 and 5, biased and random diffusion of gas atoms to grain boundaries; 6, loss of gas atoms due to grain boundary sweeping; 7, gas atom generation due to fission; and 8-10, the gain of gas atoms due to gas atom re-solution from intragranular, grain face and grain edge bubbles.

The 5th term on the RHS of Eq. (2), the flux of gas atoms randomly diffusing to the grain boundaries, is obtained by solving for the concentration of gas atoms, C_g, within the spherical grain satisfying the equation

$$\frac{\partial C_g}{\partial t} = \frac{1}{r^2}\frac{\partial}{\partial r}\left(D_g r^2 \frac{\partial C_g}{\partial r}\right) + \beta\dot{f} . \tag{3a}$$

In general, Eq. (3a) is solved with the boundary conditions

$$C_g = 0 \quad \text{at} \quad t = 0 \quad \text{for} \quad 0 \leq r \leq d_g/2 \ , \tag{3b}$$

$$C_g = 0 \quad \text{at} \quad r = d_g/2 \quad \text{for} \quad t_o \leq t \leq t_o + h \ , \tag{3c}$$

$$\frac{\partial C_g}{\partial r} = 0 \quad \text{at} \quad r = 0 \quad \text{for} \quad t_o \leq t \leq t_o + h \ , \tag{3d}$$

where h is the time increment.

The concentration of gas atoms in a spherical grain described in Eq. (3a) is written as $C_g^o(r)$ at a time t. After a small time interval, δt, the concentration becomes $C_g(r)$. Using the backward Euler approximation, for small δt, Eq. (3a) may be replaced by

$$\frac{1}{r^2} \frac{d}{dr}\left(D_g r^2 \frac{dC_g}{dr}\right) - \frac{C_g}{\delta t} + \frac{C_g^o}{\delta t} + \beta \dot{f} = 0 \ . \tag{4}$$

Euler's theorem may now be used to obtain a variational principle equivalent to Eq. (4):

$$\delta \int_0^{\frac{1}{2}d_g} 4\pi\left[\frac{D_g}{2}\left(\frac{dC_g}{dr}\right)^2 + \frac{C_g^2}{2\delta t} - \left(\frac{C_g^o}{\delta t} + \beta\dot{f}\right)C_g\right] r^2 dr = 0 \ , \tag{5}$$

which assumes that Dirichlet boundary conditions are to be applied. An approximate solution to the problem may now be obtained by choosing a trial function that satisfies the boundary conditions and minimizes the integral in Eq. (5) in terms of free parameters in the function. Many types of trial function could be chosen, but piece-wise functions are easier to handle than global functions. Quadratic functions are attractive as they allow an exact

representation of Eq. (3a) for long times. To meet the objective of a realistic level of accuracy with a minimum of computer storage and running time, the spherical grain is split into two concentric regions of approximately equal volume. In each region, the gas concentration is represented by a quadratic function.

The solution to Eq. (3a) obtained in this manner has been shown[5] to agree quite well with the solution obtained from a more detailed finite elemental analysis.

The last three terms on the RHS of Eq. (2), which account for the effects of fission-induced gas atom re-solution, depend on the rate, b, (in s^{-1}) at which gas atoms are ejected from the bubble. The rate b is calculated with the assumption that gas-atom re-solution from a spherical bubble is isotropic and proceeds by the knocking out of single gas atoms. Thus,

$$b = \frac{3b_o \dot{f}}{R^3} \int_{R-\lambda}^{R} \left(\frac{1 + \cos\theta}{2}\right) r^2 dr , \tag{6a}$$

where $\cos\theta = (R^2 - \lambda^2 - r^2)/2r\lambda$. A straightforward integration of Eq. (6a) results in

$$b = \frac{3b_o \dot{f}}{R^3}(F_2 - F_1) , \tag{6b}$$

where

$$F_2 = R^2 \left[\frac{R}{6} + \frac{R^2}{16\lambda} + \frac{1}{8}\left(\lambda - \frac{R}{\lambda}\right)\right] , \tag{6c}$$

$$F_1 = (R - \lambda)^2 \left[\frac{R - \lambda}{6} + \frac{(R - \lambda)^2}{16\lambda} + \frac{1}{8}\left(\lambda - \frac{R}{\lambda}\right)\right] . \tag{6d}$$

λ is the average distance an ejected atom travels, b_o is a measurable property of the material, and δ is a measure of the "strength" of gas atom re-solution from grain boundary bubbles.

In order to solve for C_g, using Eq. (2), a number of terms on the RHS have to be determined. RHS terms 2, 3, 6, and 8 depend on C_b. The equation for C_b, the concentration of intragranular bubbles, is given by

$$\frac{dC_b}{dt} = 16\pi F_N R_g D_g C_g^2/N_b + 4\pi(D_g + D_b)(R_g + R_b)C_g C_b/N_b$$

$$+ \pi|V_b - V_g|(R_g + R_b)^2 C_g C_b/N_b - S_v^{\alpha\alpha} V_b C_b$$

$$+ \frac{6D_b}{d_g} \frac{\partial C_b}{\partial r}\bigg|_{r=d_g/2} - \pi C_b d_g^2(t)V_{gb}/2 - bC_b$$

$$+ \frac{3V_{gb}}{d_g}N_b\left(\frac{K_f}{N_f}\dot{C}_f + \frac{K_e}{N_e}\dot{C}_e\right). \tag{7}$$

The first 6 terms on the RHS of Eq. (7) have analogous interpretations to those given for Eq. (2). The last term accounts for the introduction of grain face and grain edge bubbles into the lattice due to bubble pulloff (if the bubbles are bigger than a given critical size) from a moving grain boundary, and/or the presence of large temperature gradients.

Intergranular fission gas: grain faces

Six basic quantities still need to be determined before Eqs. (2) and (7) can be solved: N_b, N_f, N_e, C_f, C_e, and V_{gb}, the velocity of a moving grain boundary. The equation for C_f, the concentration of gas bubbles on the grain faces (assuming that the grains have an approximate tetrakeidecahedral structure), is given by

$$\frac{dC_f}{dt} = -\delta b C_f - \frac{3V_{gb}}{d_g} K_f C_f - V_f \cdot (\text{area/vol}) C_f$$

$$- V_f \cdot \sqrt{14}/d_g C_f - P_A C_f/t + S_v^{\alpha\alpha}(V_g C_g/N_f + V_b C_b N_b/N_f)$$

$$- \frac{6}{d_g}\left[\frac{D_g}{N_f}\frac{\partial C_g}{\partial r}\bigg|_{r=d_g/2} + \frac{D_b N_b}{N_f}\frac{\partial C_b}{\partial r}\bigg|_{r=d_g/2}\right]$$

$$+ \pi d_g^2(t)V_{gb}(C_g/N_f + C_b N_b/N_f)/2 \ . \tag{8}$$

The 1st and 2nd terms on the RHS of Eq. (8) are loss terms due to bubble destruction by gas atom re-solution, and bubble pulloff, respectively. The 3rd term on the RHS of Eq. (8) is the loss of grain face bubbles due to biased migration out of the node (area = cross sectional area of node boundary, and vol = volume of node; in general, for solid fuel, a node has the shape of a cylindrical annulus). The 4th and 5th terms represent the biased migration, and migration of grain face gas through grain face channels to the grain edges.

FASTGRASS calculates grain face saturation by fission gas by dealing directly with the calculated fission gas bubble distributions. The projected areal coverage of the grain face by these bubbles, per unit volume, is given by

$$A = \pi R_f^2 C_f f_f(\theta) \ , \tag{9}$$

where $f_f(\theta)$ is a geometrical factor which accounts for the lenticular shape of the grain face bubbles. If the gas is assumed to occupy equal, closely packed, touching bubbles, the maximum areal coverage per unit area of grain

face is A* = 0.907. (Under conditions where this assumption is not valid, $A^* < 0.907$, the FASTGRASS code utilizes the value A* = 0.50.) Grain face saturation (i.e., the initiation of gas-channel formation) occurs when

$$A \geq A^* S_v^{\alpha\alpha} , \qquad (10)$$

where $S_v^{\alpha\alpha}$ is the grain face area per unit volume.

Equations (9) and (10) do not account for local variations in the fuel microstructure. To include these effects in the calculation of grain face channel formation, it is assumed that the local variations in fuel microstructure can be represented by the width, σ_b, of a distribution of A [Eq. (9)] such that the grain face channel interlinkage fraction is given by

$$P_A = \frac{1}{\sigma_b \sqrt{2\pi}} \int_{x=A^* S_v^{\alpha\alpha}} \exp\left[-(x - A)^2/2\sigma_b^2\right] dx . \qquad (11)$$

The width of the distribution in Eq. (11) is a function of erratic structural parameters, depending on the local fuel condition and heterogeneity; in principle, it can be determined experimentally.

Intergranular fission gas: grain edges

The equation for C_e, the grain-edge bubble concentration, is given by

$$\frac{dC_e}{dt} = -\delta b C_e - 3V_{gb} K_e C_e + V_f \frac{\sqrt{14}}{d_g} \frac{N_e}{N_f}(1 - P_I)C_f$$

$$+ P_A \frac{N_e}{N_f}(1 - P_I)C_f/t - \frac{dP_I}{dt}C_e . \qquad (12)$$

In Eq. (12), the last term on the RHS represents the loss of gas due to release through long-range interconnection of grain edge porosity to a free

surface. The FASTGRASS model for calculating the probability of long-range grain edge tunnel interconnection is based on the assumption that the long-range interconnection is a function of the grain edge bubble swelling. To account for local fluctuations in fuel microstructure and gas bubble morphology, the grain-edge-porosity interlinkage fraction, P_I, is assumed to be a statistical distribution around an average value of the grain edge swelling, B_{vedge}:

$$P_I = \frac{1}{\sigma_E \sqrt{2\pi}} \int_{x=B_{vcrit}}^{\infty} \exp[-(x - B_{vedge} - B_{vpor})^2 / 2\sigma_E^2] dx . \tag{13}$$

where $B_{vedge} = 4/3\pi R_e^3 f_e(\theta) C_e$, and $f_e(\theta)$ is a geometrical factor which accounts for the ellipsoidal shape of grain-edge bubbles. $B_{vcrit} = 0.05$ is the value of grain edge swelling at which long-range interconnection would take place if the fuel microstructure and gas bubble morphology were homogeneous; $B_{vpor} = 0.0$ for $\rho \geq 92\%$ of theoretical density. In the absence of microcracking, the fission gas that would have been vented via the crack remains on the grain boundaries. (FASTGRASS has a model for intergranular microcracking due to overpressurized fission gas bubbles. This model has been discussed in a previous paper.[2] The effects of microcracking on interlinkage are included by redefining P_I: $P_I = $ maximum (P_I, M_c), where M_c is the fraction of the grain boundary area/volume which has opened up due to microcracking.) Retained grain edge fission gas causes the deformation of the grain edges (i.e., grain edge fission-gas-bubble swelling), and the subsequent increased long-range interconnection of grain edge tunnels. This interconnection of grain edge tunnels provides the pathways for enhanced fission gas release.

Calculation of N_b, N_f, and N_e

Equations (2), (7), (8) and (12) express mass balance and are solved by assuming that the average number of atoms per bubble does not change over the integration time step, i.e., $\dot{N}_b = \dot{N}_f = \dot{N}_e = 0$. Subsequent to the calculation of the C_is, changes in N_i are calculated by examining the bubble growth and shrinkage fluxes that influence the average size bubble. For example, changes in N_b are calculated by evaluating

$$\dot{N}_b \propto \frac{1}{C_b}\left[16\pi R_b D_b C_b^2 + \pi R_b^2 \alpha_b V_b C_b^2\right.$$

$$+ 4\pi(D_g + D_b)(R_g + R_b)C_g C_b/N_b - bC_b$$

$$\left. - 16\pi F_N R_g D_g C_g^2 + \frac{3V_{gb}N_b}{d_g}\left(\frac{K_f}{N_f}C_f + \frac{K_e}{N_e}C_e\right)\right]. \tag{14}$$

In Eq. (14), the first 3 terms on the RHS correspond to the growth of the average size bubble due to random and biased coalescence of these bubbles with each other, and the growth of these bubbles due to accumulation of gas atoms. The 4th and 5th terms on the RHS of Eq. (14) represent the shrinkage of the average size bubble due to bubble destruction by fission-induced gas atom re-solution, and due to the generation of very small bubbles by gas-atom nucleation (i.e., the introduction of small bubbles will tend to weight the average size bubble toward smaller sizes). The last two terms represent the growth of the average size bubble by introducing into the lattice larger grain face and grain edge bubbles which have become detached from the moving grain boundary. The proportionality sign in Eq. (14) indicates that the changes in N_b are computed using a numerical algorithm which evaluates Eq. (14) and increments or decrements N_b by an amount proportional to this value. When N_b

is calculated in this fashion, it agrees very well with the results of calculations for the evolution of the bubble size distribution made with the GRASS-SST mechanistic model.[6] The equations for $\dot{N}_f$ and $\dot{N}_e$ are obtained in an analogous fashion to Eq. (14).

Fission gas release

Contributions to fission gas release, g, come from the venting of grain face gas into interconnected grain edge tunnels, from the venting of previously trapped grain-edge gas through newly interconnected tunnels, and from the long-range migration of fission gas bubbles up the temperature gradient:

$$\frac{dg}{dt} = \left\{ \frac{V_f\sqrt{14}}{d_g} C_f + P_A C_f/t \right\} P_I + C_e \frac{dP_I}{dt} + V_f(\text{area/vol})C_f \tag{15}$$

For a multinode calculation, the various gas release contributions from each individual node, given by Eq. (15), are summed up to obtain the total gas released during time t. The total contribution of gas released due to long-range migration of fission gas bubbles up the temperature gradient depends on the cross-sectional area of the inner or outer node depending on the direction of the gradient which bounds a free surface.

Calculation of bubble radii

The intergranular gas bubbles are assumed to be lenticular on the grain faces and ellipsoidal along the grain edges. Grain corner bubbles are grouped with edge bubbles and are assumed to have the same shape.

The diffusional growth of nonequilibrium intragranular bubbles is based on an analysis by Gruber.[7] The rate of change of the bubble radius is given by

$$\frac{dR_b}{dt} = \frac{D_u}{R_b}\left[1 - \exp\text{-}(P - P_h - \frac{2\gamma}{R_b})\frac{\Omega}{kT}\right] \;, \tag{16}$$

where D_u is the vacancy diffusion coefficient; Ω, is the atomic volume; kT, the thermal energy; P, the internal gas pressure; P_h, the external hydrostatic pressure; and γ, the surface energy. For ease in calculating, Gruber provided a relaxation time approximation of the form:

$$R_b = R_b^o + (R_b^{eq} - R_b^o)(1 - e^{-t/\tau}) \;, \tag{17}$$

where τ is defined by the initial growth rate calculated using Eq. (16). In FASTGRASS R_b^{eq} is obtained by solving Harrison's extrapolated equation of state simultaneously with the capillarity relation.

The diffusional growth of non-equilibrium intergranular bubbles is taken from Speight and Beere.[8] Accordingly, the rate of volume change of grain boundary pores is given by:

$$\frac{dV}{dt} = \frac{2D_{gb}W}{kTL}\left(P - \frac{2\gamma}{\rho} - P_h\right) \;, \tag{18}$$

where V is the volume of the pore, ρ is the radius of curvature of the pore, L is a function of the area fraction of the grain boundary occupied by pores, D_{gb} is the grain boundary diffusion coefficient, and W is the boundary thickness.

Grain-growth effects

FASTGRASS has recently been used[3] in the interpretation of fission gas (as well as I, Cs and Te) release data from Oak Ridge National Laboratory (ORNL)[9] electrical heating experiments, where normally irradiated ($\approx 30,000$ MWd/t) spent fuel (removed from the reactor more than 10 years earlier) was

tested in a flowing steam environment. It was also used in the interpretation of the in-reactor data for PBF trace-irradiated ($\simeq$90 MWd/t) and normally irradiated (~30,000 MWd/t) fuel.[10] The results of these analyses demonstrate that intragranular fission product behavior during both types of tests can be interpreted in terms of a solid-phase grain growth/grain-boundary-sweeping mechanism (T > 1900 K) that enhances the flow of fission products from within the grains to the grain boundaries.[11] Basically, the model assumes that small intragranular bubbles (consisting, in general, of Xe, Kr, I, Cs, and CsI), and gaseous and VFP atoms in the path of a growing grain, are swept up by grain boundary adhesive forces. Such grain boundary sweeping provides another mechanism for the collection of fission products at grain faces and edges during solid-phase fuel heat-up.

The FASTGRASS theory of grain boundary sweeping of gas bubbles[3] considers the effects on the moving boundary of two distinct distributions of bubble sizes; those on the grain faces and those on the grain edges. The motion of the moving boundary is retarded by the presence of both grain face and grain edge bubbles. The force exerted by the bubbles on the boundary, F_b, depends on bubble radius and angle of contact, and can be expressed according to the relationship

$$F_b = \pi R_f n_f \gamma_{gb} \sin 2\phi_f + \pi R_e n_e \gamma_{gb} \sin 2\phi_e \equiv n_f F_f + n_e F_e, \qquad (19)$$

where ϕ_f and ϕ_e are the angles of contact between the bubbles and the boundary; n_f and n_e are the corresponding number of bubbles; γ_{gb} is the grain boundary surface tension; and, F_f and F_e represent, respectively, the forces exerted by a grain face and grain edge bubble on the boundary.

The velocity of these bubbles can be determined from the individual forces on the bubbles by utilizing the Nernst-Einstein equation. Assuming that bubbles at grain boundaries move by surface diffusion, the velocity is

$$V_f = \frac{D_f F_f}{kT} = \frac{3}{4} \frac{a_o^4 D_o}{R_f^3} \frac{2\gamma_{gb}}{kT} \sin 2\phi_f \exp\left(\frac{-E_s}{kT}\right) , \qquad (20)$$

and

$$V_e = \frac{D_e F_e}{kT} = \frac{3}{4} \frac{a_o^4 D_o}{R_e^3} \frac{2\gamma_{gb}}{kT} \sin 2\phi_e \exp\left(\frac{-E_s}{kT}\right), \qquad (21)$$

where a_o is the lattice constant; D_o is the preexponential factor for surface self-diffusion of the matrix solid; and E_s is the activation energy for this process.

It has previously been shown[3] that the grain boundary velocity in the presence of gas bubbles is given by

$$V_{gb} = \frac{2a_o^4 \nu \gamma_{gb}}{r_c kT} \exp(-Q/kT)\left[1 - \frac{1}{2}\left(\frac{\pi C_f R_f^2}{S_v^{\alpha\alpha}}\right)\left(\frac{r_c}{R_f}\right) \sin 2\phi_f\right.$$

$$\left. - \frac{1}{2}\left(\frac{\pi C_e R_e^2}{S_v^{\alpha\alpha}}\right)\left(\frac{r_c}{R_e}\right) \sin 2\phi_e\right] , \qquad (22)$$

where ν is the frequency of vibration of an atom in the solid lattice adjacent to the boundary, r_c is the radius of curvature of the grain, and Q is the activation energy for grain boundary motion. If $V_e = V_b$ and $V_f = V_{gb}$, the grain face and grain-edge bubbles are swept along with the moving boundary. If this condition does not hold, the grain edge and/or grain face bubbles are pulled off the moving boundary and are reintroduced into the grain lattice
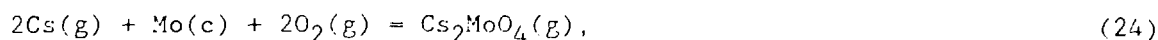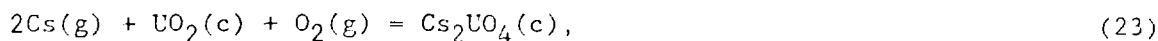
boundary and are reintroduced into the grain lattice [see Eqs. (2), (7), (8), and (13)].

When the bubbles are widely spaced or very small, the second and third terms in the brackets in Eq. (22) are negligible compared to unity, and V_{gb} reduces to the intrinsic velocity of the curved grain boundary. The second and third terms in the brackets in Eq. (22) account for the retarding effects of the bubbles on grain boundary motion.

UO_2-fission product chemistry

The FASTGRASS model for reactive VFP and AEFP release is based on two major assumptions: (1) as the VFPs and AEFPs are known to react with other elements to form compounds, a realistic description of VFP/AEFP release must include the effects of chemistry on behavior, and (2) as the noble gases have been shown to play a major role in establishing the interconnection of escape routes from the interior to the exterior of the fuel, a realistic description of VFP/AEFP release must include, a priori, a realistic description of fission gas release and swelling. The physical reasonableness of these assumptions has been supported, thus far, by good agreement between model predictions and actual observation.

Based on the work of Tam et al.,[12] the following system of equations is used to assess Cs and I sequestering behavior in UO_2 fuel:

$$2Cs(g) + UO_2(c) + O_2(g) = Cs_2UO_4(c), \tag{23}$$

$$2Cs(g) + Mo(c) + 2O_2(g) = Cs_2MoO_4(g), \tag{24}$$

$$Cs + I = CsI, \tag{25}$$

where g and c designate gas and crystalline phases, respectively.

Tellurium (Te) is considered non-reactive within the fuel matrix. The physical basis for the primary reactions governing the chemical behavior of I and Cs in UO_2-based fuel is reasonably well established and documented in the literature (Refs. 12-14). However, the internal fuel rod chemistry governing Ba and Sr release is less certain and no mechanistic model exists at this time for the estimation of the release behavior of Ba and Sr, from severely damaged fuel. Rather, the release of these fission products is based solely on empirical correlations obtained from a limited data base. Here we postulate a basis for estimation of such Ba and Sr release.
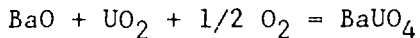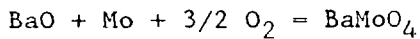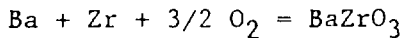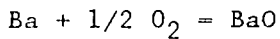
Barium and strontium belong to the Group II (alkaline earth) elements. As discussed in Ref. 15, evidence indicates that Ba and Sr may be present in the fuel as simple oxides, uranates, molybdates, or zirconates. The simple oxides and the molybdates would be the most stable of these compounds; compounds formed with Sr tend to be more stable than the corresponding Ba compounds. In general, the formation of such compounds can be expected to immobilize Ba and Sr within the fuel matrix, and thus limit their release potential. Therefore, of particular interest with respect to release modeling is the establishment of a basis for estimating of the amount of Ba and Sr that remains in the more mobile elemental form or in a vapor phase (e.g., within fission gas bubbles), versus the quantities of these fission products that react to form less volatile species.

A qualitative guide to the chemical state of fission product Ba and Sr in oxide fuel is their affinity for oxygen. The stability of fission product Ba and Sr as elements or as oxides in the presence of UO_2 depends on the difference between the free energy of the fission product oxide and the fuel oxygen potential. For fission product compounds with free energies below that of the fuel oxygen potential, an oxide is predicted; for compounds with free
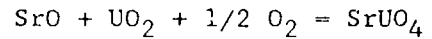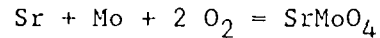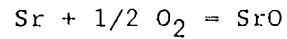
energies above that of the fuel oxygen potential, a stable element is predicted. Comparison of the oxygen potential of stoichiometric UO_2 fuel with the free energies of formation of Ba and Sr fission product oxides clearly indicates that Ba and Sr have a high propensity to form oxides. Stoichiometry also plays an important role: hyperstoichiometric fuel tends to show an enhanced potential for the formation of fission product oxides.

The Ba and Sr reactions of interest are as follows:

Barium

$Ba + 1/2\ O_2 = BaO$

$Ba + Zr + 3/2\ O_2 = BaZrO_3$

$BaO + Mo + 3/2\ O_2 = BaMoO_4$

$BaO + UO_2 + 1/2\ O_2 = BaUO_4$

Strontium

$Sr + 1/2\ O_2 = SrO$

$Sr + Mo + 2\ O_2 = SrMoO_4$

$SrO + UO_2 + 1/2\ O_2 = SrUO_4$

It should be noted that the alkaline earths also exhibit the potential to form iodides. However, since high-yield Cs has a higher free energy of formation with I than do Ba and Sr, the potential for CsI formation is greater, and tends to limit the formation of Ba and Sr iodides. Thus, for all practical purposes, the above reactions can be expected to control the internal fuel rod chemistry of Ba and Sr. The free energies of formation, ΔG, for some of the above reactions, and for several relevant Cs reactions, are presented in Table 3; they are based upon values suggested in Ref. 16.
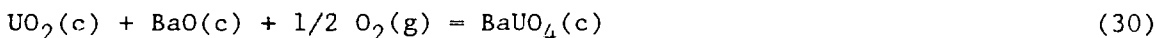
In addition to the formation of oxides, uranates, molybdates, and zirconates, which can be expected to be dispersed throughout the fuel matrix, evidence exists that Ba and Sr may aggregate into inclusions which effectively form a separate phase within fuel (i.e., physical and chemical properties determined by inclusion composition rather than fuel properties). However,

the consensus of various researchers is that both Ba and Sr, in normally irradiated fuel, exist primarily in the fuel matrix in oxide form and not as a prime constituent of metallic inclusions. Because of uncertainties in composition, oxidation state, homogenity, and the indication that Ba and Sr are not major inclusion constituents, Ba and Sr holdup via metallic inclusion sequestering will not be considered in this analysis. Indeed, one would expect that inclusions containing Ba and Sr would be primarily of the oxide form rather than metallic.

Equilibrium fission product distributions for the various phases of the fuel/fission-product system at 1500 K have been calculated.[15,16] The calculations are based on UO_2 fuel at 2 at.% burnup, an oxygen-to-uranium ratio that is slightly hyperstoichiometric, and a 10% void volume in the fuel. Such an equilibrium distribution may not be achieved at 1500 K in a transient sequence, since the release of the fission products to voids and bubbles may be too slow. Moreover, the estimates of solutions of fission product oxides in urania are based on sparse data. In spite of these limitations, thermochemical equilibrium calculations indicate that the most probable distribution of Ba and Sr in the UO_2 is as follows:

Barium Partitioning in UO_2		Strontium Partitioning in UO_2	
BaO	59%	SrO	96%
$BaUO_4$	35%	$SrMoO_4$	4%
$BaMoO_4$	4%		
$BaZrO_4$	2%		

In view of the thermochemical conditions in fissioned UO_2 fuel discussed above, FASTGRASS assumes that the following reactions dominate Sr and Ba sequestering effects within the UO_2 matrix:

$$Sr(s) + 1/2 \; O_2(g) = SrO(c) \tag{26}$$

$$SrO(c) = SrO(g) \tag{27}$$

$$Ba(s) + 1/2 \; O_2(g) = BaO(c) \tag{28}$$

$$BaO(c) = BaO(g) \tag{29}$$

$$UO_2(c) + BaO(c) + 1/2 \; O_2(g) = BaUO_4(c) \tag{30}$$

where s represents atoms in solution, and c and g represent crystalline and gas phases, respectively.

For the Sr and Ba reactions, the concentration of nine chemical species [Sr, SrO(c), SrO(g), O_2, Ba, BaO(c), BaO(g), $BaUO_4$(c), and UO_2] must be determined in order to specify the fraction of fission product Sr and Ba that is available for release from the fuel matrix either in atomic form, or as an oxide. Six additional chemical species result from the I and Cs reactions (I, Cs, CsI, Cs_2UO_4, Cs_2MoO_4, and Mo). From the law of mass balance, the total fractional atom concentration of Sr, Ba, Cs, I, and Mo equals the sum of their respective fission yields, i.e.,

$$C_{Sr}^T = C_{Sr} + C_{SrO(c)} + C_{SrO(g)} = 0.0926 \; B \; , \tag{31}$$

$$C_{Ba}^T = C_{Ba} + C_{BaO(c)} + C_{BaO(g)} + C_{BaUO_4} = 0.0682 \; B \; , \tag{32}$$

$$C_{Cs}^T + C_{Cs} + C_{CsI} + 2C_{Cs_2UO_4} + 2C_{CsMoO_4} = 0.1882 \; B \; , \tag{33}$$

$$C_I^T = C_I + C_{CsI} = 0.011 \; B \; , \tag{34}$$

$$C_{Mo}^T = C_{Mo} + C_{Cs_2MoO_4} = 0.2348 \; B \; , \tag{35}$$

where C_i^T = total fractional concentration of species i (e.g., Sr, Ba) generated as a function of fractional burnup B, and C_i = fractional concentration of the individual chemical forms of species i. The concentrations of O_2 and UO_2 can be assessed from standard models as a function of temperature, O/U ratio, burnup, and fuel density; thus, seven of the fifteen concentrations are known. The eight remaining equations can be obtained from the law of mass action. For the reaction(s) Sr + 1/2 O_2(g) = SrO(c), Eq. (26), the equilibrium constant, K_1 can be expressed in terms of the free energy of formation, ΔG and the concentration of the reactants and products; i.e.,

$$K_1 = \exp\frac{-\Delta G_1}{RT} = \frac{a_{SrO(c)}}{c_{Sr} P_{O_2}^{1/2}} , \qquad (36)$$

where ΔG_1 is obtained from Table 3; P_{O_2} is the oxygen partial pressure; and $a_{SrO(c)}$ is the activity of SrO(c). For the reaction Ba(s) + 1/2 O_2(g) = BaO(c), Eq. (28), the equilibrium constant, K_2 can be similarly expressed as

$$K_2 = \exp\frac{-\Delta G_2}{RT} = \frac{a_{BaO(c)}}{c_{Ba} P_{O_2}^{1/2}} . \qquad (37)$$

The remaining six equations [Eqs. (23-25, 27, 29-30)] can be expressed in terms of the corresponding free energies of formation and concentrations of the reactants and products in a similar manner.

In order to utilize the free energies given in Table 3 for the reactions described by Eqs. (26) and (28), one needs to know the corresponding solution energies for Ba and Sr. The values used in this analysis for Ba and Sr are 46,700 and 33,000 cal/mol, respectively.

Table 3. Free Energy of Formation of Ba and Sr Fission Product Oxides

Reactants[a]	Product	Free Energy, ΔG (cal/mol Product)	Temperature (K)
Barium			
$Ba(c) + 1/2\ O_2(g)$	$BaO(c)$	$-117713 + 16.7T$	298-983
$Ba(l) + 1/2\ O_2(g)$	$BaO(c)$	$-133186 + 24.56T$[b]	983-2122
$Ba(c) + 1/2\ O_2(g)$	$BaO(g)$	$-31367 - 12.95T$	298-983
$Ba(l) + 1/2\ O_2(g)$	$BaO(g)$	$-38373 - 6.76T$	983-2268
$BaO(c)$	$BaO(g)$	$98138 - 33.21T$	-
$Ba(c) + U(c) + 2O_2(g)$	$BaUO_4(c)$	$-473010 + 87.3T$	298-1403
$UO_2(c) + BaO(c) + 1/2\ O_2$	$BaUO_4(c)$	$-81517 + 22.32T$	-
Strontium			
$SrO(c)$	$SrO(g)$	$135344 - 36.42T$	298-2938
$Sr(c) + 1/2\ O_2(g)$	$SrO(c)$	$-141156 + 22.92T$	298-1041
$Sr(l) + 1/2\ O_2(g)$	$SrO(c)$	$-142835 + 24.55T$	1041-1654
$Sr(g) + 1/2\ O_2(g)$	$SrO(c)$	$-174079 + 43.44T$	1654-2938
Cesium			
$Cs(g) + I(g)$	$CsI(g)$	$-73041 + 15.81T$	-
$2Cs(g) + UO_2(c) + O_2(g)$	$Cs_2UO_4(c)$	$-233152 + 91.62T$	-
$2Cs(g) + Mo(c) + 2O_2(g)$	$Cs_2MoO_4(g)$	$-325372 + 86.52T$[c]	952-2892

[a] c, g, and l designate crystalline gas, and liquid phases, respectively.
[b] The value of ΔG listed in Ref. 16 is incorrect.
[c] The value of ΔG used in this analysis is $\Delta G = -297715 + 79.166T$.

The activities of the various reaction products in a condensed phase can be written as an activity coefficient times the concentration of the reaction product [e.g., $a_{BaO(c)} = \alpha_{BaO(c)} C_{BaO(c)}$]. It is assumed that all the condensed-phase Ba, Sr and Cs reaction products are distributed uniformly within the UO_2 matrix, so that $\alpha_i = 1$, where i denotes the particular reaction product.

Following the analysis of CsI formation in UO_2 given by Cronenberg and Osetek,[17,18] it is assumed that the formation of the reaction products CsI(g), SrO(g), and BaO(g) requires the presence of reaction sites, which are primarily microbubbles containing the noble fission gases Xe and Kr.

The activities of the gas-phase reaction products [i.e., CsI(g), BaO(g), and SrO(g)] are equal to their corresponding partial pressures, P_{CsI}, P_{BaO}, and P_{SrO}. Once these partial pressures have been calculated, they can be used in conjunction with an equation of state of the Van der Waals form,

$$P(V_b - b) = nRT \tag{38}$$

[where b is the Van der Waals constant, V_b is the bubble volume, and n is the number of atoms of CsI(g), SrO(g) or BaO(g) in the bubble in atoms/cm^3], to calculate the quantity of CsI(g), SrO(g) and BaO(g) in the material. As the bubble volume, V_b, is calculated directly in FASTGRASS, there are no remaining unknowns in this calculation.

The oxygen partial pressure is calculated according to the analysis of Blackburn and Johnson, and is given by the following expression:

$$P_{O_2}^{1/2} = \frac{(\phi - 2) + [(\phi - 2)^2 + 4B(3 - \phi)(\phi - 1)/A]^{1/2}}{2B(3 - \phi)/\phi} , \tag{39}$$

where $A = \exp(78300/T - 13.6)$, $B = \exp(16500/T - 5.1)$, and $\phi = O/U$.

The value of ϕ can be calculated by taking into account the fissioning of ^{235}U and the formation of the oxides and uranates given in Eqs. (23-32), i.e.,

$$\phi = \phi_o + \frac{\dot{f}t}{N_m^o}(\phi_o - \alpha) - \alpha, \qquad (40)$$

where $\alpha = C_{SrO(c)} + C_{SrO(g)} + C_{BaO(c)} + C_{BaO(g)} + C_{BaUO_4} + 2C_{Cs_2UO_4} + 4C_{Cs_2MoO_4}$, N_m^o is the initial number of heavy metal atoms, t is the irradiation time, and ϕ_o is the starting O/U ratio. In general, as $\dot{f}$ and T are functions of time, Eq. (40) is phrased in differential form and integrated over time.

Simultaneous solution of this coupled system of equations [Eqs. 23-35, 39-40] yields the equilibrium concentrations as a function of fuel burnup and temperature. The amount of Sr and Ba that is predicted to be retained in the fuel in atomic form or in the vapor phase in microbubbles is assumed available for release, whereas all other species are assumed to be immobilized within the fuel microstructure.

Once the fractions of atomic Sr and Ba are known, their mobility through the fuel microstructure is assessed. CsI(g), BaO(g) and SrO(g) are assumed to migrate within fission gas bubbles. The migration of atomic I, Cs, Ba, and Sr are handled in an analogous fashion to that of the noble gases: the concentrations of these species within the grains and on the grain boundaries are described using equations of the form shown by Eq. (1). Cs, I, Sr and Ba gas atom diffusivities are taken to be the same as that of Xe. The specific variables associated with these equations are defined in Table 2. These calculations for fission product chemistry and migration are performed sequentially, as a function of time. This method of calculating VFP/AEFP behavior is reasonable as long as the integration time steps are chosen small enough so that a quasi-chemical equilibrium is maintained.

3. FASTGRASS Theory of Gas Bubble Behavior in Degraded Fuel

A wide range of material interaction and phase transformation phenomena can be expected at the elevated temperatures associated with severe core damage accidents; one of the more significant is the steam-cladding (Zircaloy) reaction, with ZrO_2 and oxygen-stabilized alpha-Zircaloy [α-Zr(O)] byproducts.

Liquefaction effects

Figure 1 presents the pseudobinary equilibrium phase diagram UO_2 and oxygen-saturated alpha-Zr(O). As indicated, oxygen-saturated α-Zr(O) will dissolve UO_2 if they are in contact at temperatures in excess of $\approx$2170 K. A eutectic melt is formed with a 5% mole fraction of UO_2, whereas, at higher UO_2 compositions, there exists a mixture of liquid with a $(U,Zr)O_2$ solid component that is analogous to a slush. A mixture of two liquids (i.e., $L_1 + L_2$) occurs at temperatures above $\approx$2673 K, when the UO_2 mole composition is between $\approx$23% and 85%.

Such parameters as fuel pellet microcracking, oxidation state, wetting characteristics, and time at temperature also exert a pronounced influence on the dissolution process. Until the influence of such parameters can be established from a systematic data base, modeling of dissolution effects on fission product release must, of necessity, rely primarily on empirical evidence. For present purposes two limiting conditions on fuel dissolution will be considered:

Grain boundary dissolution (2673 K > T > 2170 K) - where limited attack of molten alpha-Zr(O) on the fuel microstructure results in a residual U-rich melt phase at grain boundaries, which effectively acts as a melt pathway for the escape of fission products to the pellet surface.
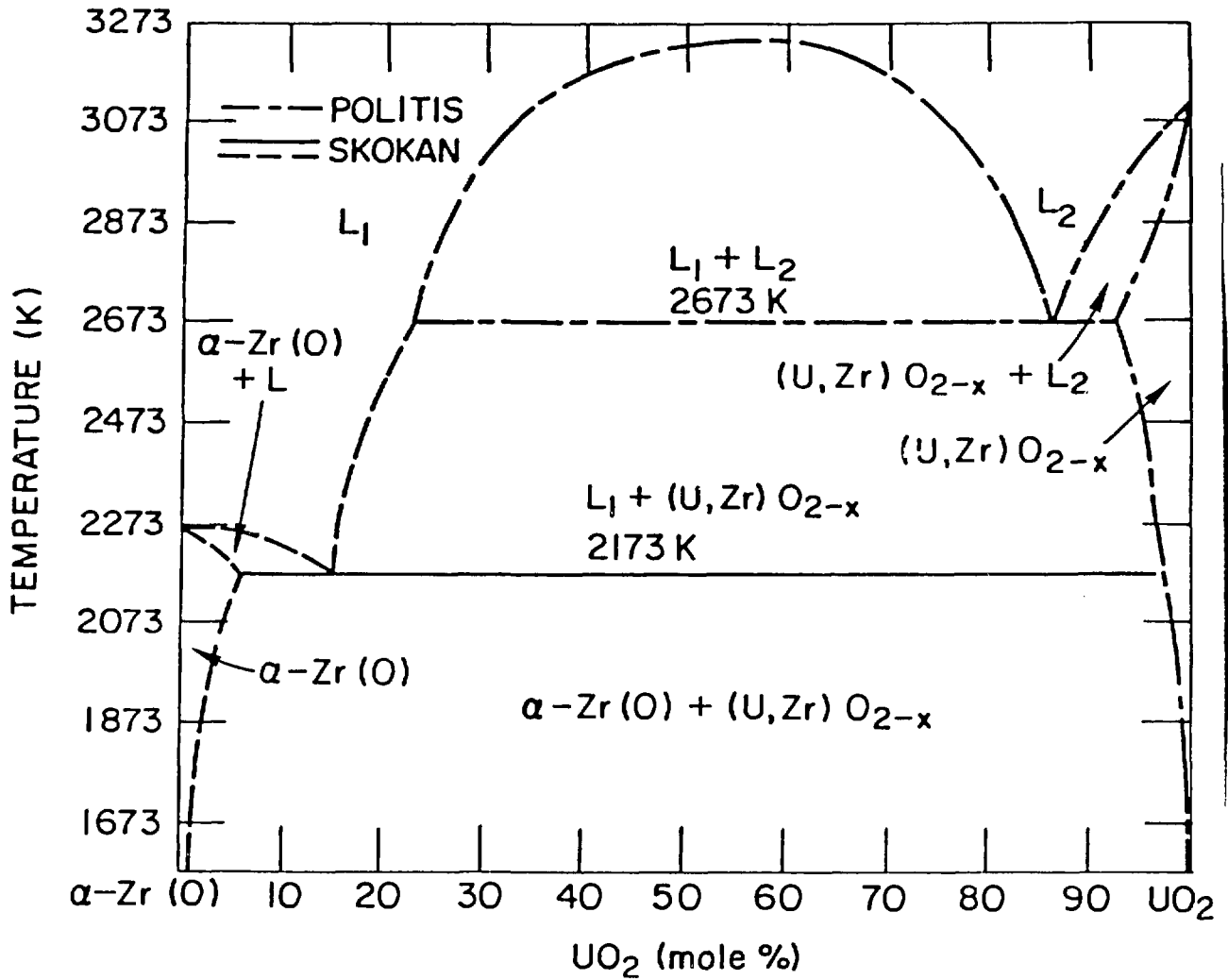
Figure 1. Equilibrium Pseudo Binary Phase Diagram of UO_2 and Oxygen-saturated Alpha-Zr(O).

Fuel matrix dissolution (T > 2673 K) - where more extensive attack of molten alpha-Zr(O) on the fuel microstructure results in dissolution of the entire grain structure over a portion of the fuel pellet radius, such that fission product transport is controlled by micro-bubble and atomic diffusion in a sea of liquefied fuel.

Models describing fission gas release behavior for these two limiting conditions have recently been developed and incorporated into FASTGRASS. For grain boundary type dissolution, release of fission products occurs primarily by fission product migration through the liquefied U, or U-Zr lamina (or film), to the fuel surface. For fuel matrix type conditions, occurs by fission product migration through the bulk melt to a free surface. Gas bubble mobility in the U/U-Zr melt can occur via bubble rise in a viscous liquid, evaporation-condensation, and volume diffusion, where the dominant mechanism is primarily dictated by bubble size.

Fuel dissolution effects

For relatively large bubbles (see Figure 2) in the absence of a strong temperature gradient, escape will be dominated by macroscopic forces, i.e., buoyancy effects, through the liquefied lamina, to the surface of the fuel (the lamina is assumed to be 1-2 μm thick and exist along the liquefied grain boundaries). This is in contrast to release processes in solid fuel, where release can occur directly upon the arrival of fission gas at the grain edges, if a stable network of interconnected porosity is encountered.

Modeling of bubble rise in a viscous liquid is based on an estimate of the pore rise time from the interior of the melt to the free surface. An approximation of the bubble velocity can be obtained by assuming that bubble interference during an increment of time is negligible and variations in properties along the distance of travel are minimal. Under such assumptions,

the classical expression for bubble rise in a viscous liquid can be employed. If a submerged, rigid bubble is allowed to rise from rest in the liquid, it will accelerate until it reaches a constant terminal velocity, V_b. In this situation, the effects of gravity, F_g and drag, F_d are just balanced by the effects of buoyancy, F_b; i.e., the equilibrium force balance for such steady-state bubble rise can be written as

$$\frac{4}{3}\pi R_b^3 \rho_L g = \frac{4}{3}\pi R_b^3 \rho_g g + 6\pi R_b \mu_L V_b, \tag{41}$$

where R_b is the bubble radius, ρ_L is the liquid fuel density, g is the gravitational constant, ρ_g is the bubble gas density, and μ_L is the viscosity of liquefied fuel.

Noting that $\rho_L \gg \rho_g$, one can express the terminal rise velocity as

$$V_{b,t} = \frac{2R_b^2 \rho_L g}{9\mu_L}. \tag{42}$$

Taking into consideration the fact that the liquid lamina can be expected to have a snake-like random structure in a partially dissolved fuel pellet, direct vertical bubble rise is unlikely. Bubble migration is, therefore, viewed as upwardly biased in a snake-like path, so that the effective rise velocity, V_t, is taken to be half (between zero and the terminal velocity) the terminal velocity, i.e. $V_b = \frac{1}{2} V_{b,t}$.

Fission gas bubbles can also migrate in the liquid by a volume diffusion mechanism. The diffusivity of a bubble of radius R_b migrating by volume diffusion is

$$D_b = \frac{3\Omega}{4\pi R_b^3} D_u, \tag{43}$$

where Ω is the molecular volume and D_u is the U-atom diffusivity. The U-atom diffusivity in molten UO_2 is based on the Sutherland-Einstein model and is given by

$$D_u = \frac{kT}{4\pi r_a \mu_L} .$$ (44)

The velocity of a bubble moving by a volume diffusion mechanism in the presence of a temperature gradient, ∇T, is expressed by

$$V_b = \frac{D_u Q_v^*}{kT^2} \nabla T ,$$ (45)

where Q_v^* is the volume diffusion heat of transport.

For larger bubbles in the presence of a relatively large temperature gradient, vapor transport can strongly dominate both buoyancy-driven bubble rise and volume diffusion. For this case, the bubble velocity is given by

$$V_b = \frac{D_v \Omega \alpha P_o \Delta H_v}{k^2 T^3} \exp\left(\frac{\Delta H_v}{kT}\right) \frac{3}{2} \nabla T ,$$ (46)

where Ω is the atomic volume; $P_o \exp\left(\frac{-\Delta H_v}{kT}\right)$ is the equilibrium vapor pressure; ΔH_v is the heat of vaporization for the rate-diffusing species of the fuel; D_v is its diffusivity in the vapor contained in the void; and $\alpha \leq 1$ measures any deviation from equilibrium vapor pressure at the pore surface. D_v is obtained from the kinetic theory of gases and is defined as follows:

$$D_v = \frac{2kT}{3\pi\sigma^2 P}\left[\frac{2kT}{\pi}\left(\frac{1}{m_1} + \frac{1}{m_2}\right)\right]^{1/2} ,$$ (47)

where $\pi\sigma^2$ is the collision cross-section between the diffusing species and the principal component of the gas phase in the void, P is the total gas pressure in the void ($P = 2\gamma/R + P_b$, where P_b = pressure in surrounding liquid and γ = surface energy), and m_1 and m_2 are the masses of the diffusing species and the principal component of the gas phase, respectively.

Figures 2 and 3 show bubble velocities as a function of bubble radius obtained by using Eqs. (42-47) at 2200 and 3125 K. Figures 2 and 3 correspond to temperature gradients of 100 and 5000 K/cm, respectively. The values of the various parameters used in the above equations are listed in Table 4.

From Fig. 2 it can be seen that for small bubbles (<1 μm) and small values of the temperature gradient (~100 K/cm), volume diffusion dominates bubble motion. On the other hand, large bubbles ($\geq$ 1 μm), in the absence of significant temperature gradients, move primarily under the forces of buoyancy. In liquid UO$_2$ with temperature gradients $\geq$ 5000 K/cm (see Fig. 3), bubbles with radii of up to about 0.1 μm move primarily by volume diffusion, while bubbles with radii greater than 0.1 μm move primarily by viscous rise.

Bubbles moving in a liquefied medium can coalesce and grow. As FAST-GRASS considers only a single bubble-size class per distinct morphological fuel region (the average-size bubble), the rate of change of the bubble density, C_b, for a bubble of radius R_b moving by random and biased migration in a liquefied lamina (e.g., a destroyed grain boundary region) is given by [see Eq. (14), and subsequent discussion]

$$\dot{C}_b = -(16\pi\,R_b D_b + \alpha\pi R_b^{\,2} V_b) C_b^{\,2} \,, \tag{48}$$

where α is a parameter that incorporates the effects of a distribution of bubble sizes, and V_b is given by either Eq. (42), (45), or (46). $\alpha = 4\pi$,
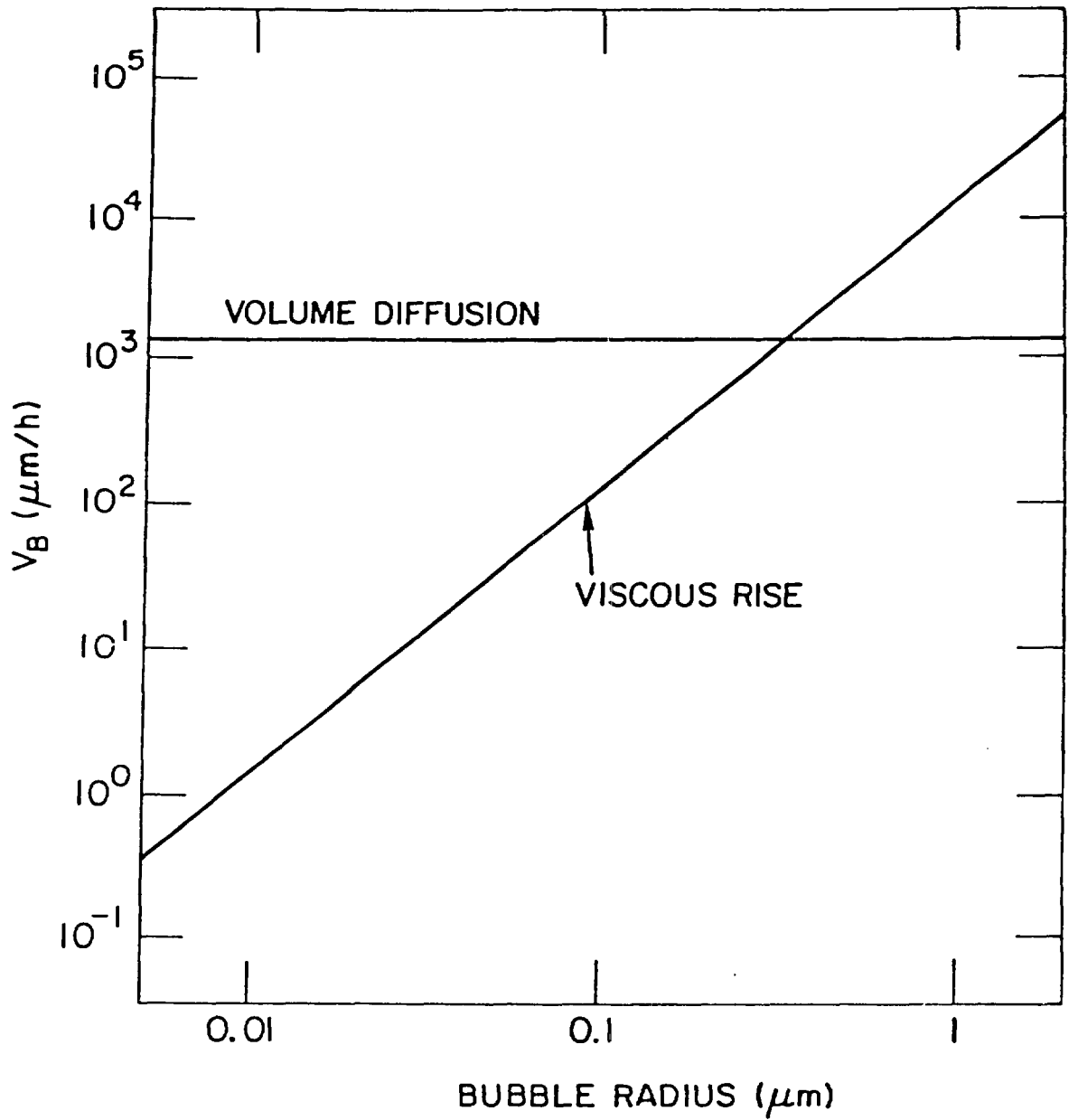
Figure 2. Size Dependence of Bubble Velocities in Liquid UO_2 in a Temperature
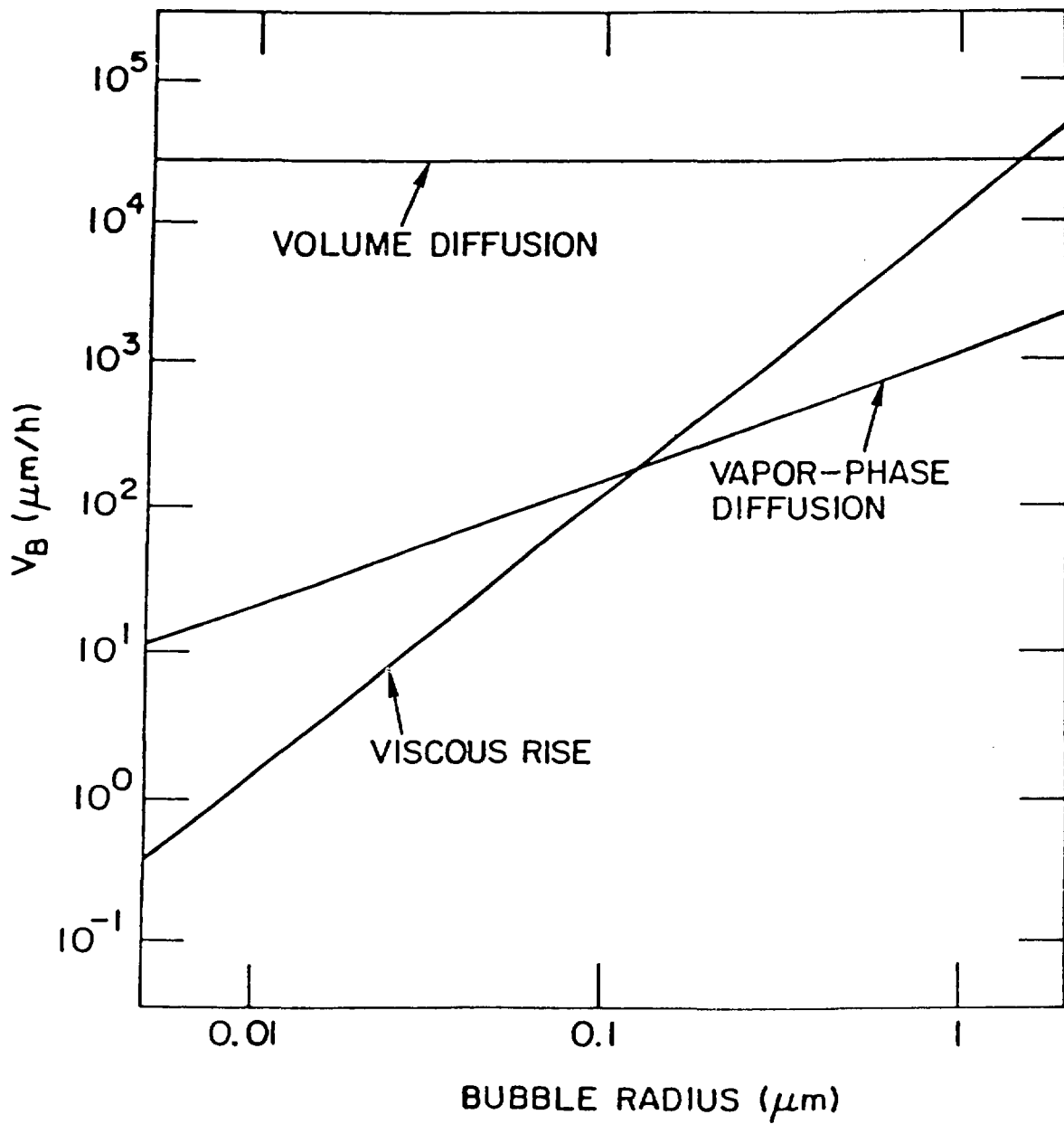Gradient of 100 K/cm at 2200 K.

Figure 3. Size Dependence of Bubble Velocities in Liquid UO_2 in a Temperature Gradient of 5000 K/cm at 3125 K.

Table 4.   Values of Various Parameters Used in FASTGRASS

Symbol	Value
ρ_L	8.74 g/cm^3
μ_L	$4 \times 10^{-2} \text{ g/s}^2$
r_a	$1.42 \times 10^{-8} \text{ cm}$
Q_v^*	$4.8 \times 10^{-12} \text{ ergs}$
P_o	$4.16 \times 10^{-4} \text{ dynes/cm}^2$
ΔH_v	$1 \times 10^{-11} \text{ ergs}$
$m_1 \text{ (UO}_2)$	$4.48 \times 10^{-22} \text{ g}$
$m_2 \text{ (Xe)}$	$2.19 \times 10^{-22} \text{ g}$
D_g	$2.1 \times 10^{-4} \, e^{-91000/RT} \text{ cm}^2/\text{s}$
D_b†	$\dfrac{1.486 \times 10^{-11} \, e^{-108000/RT}}{R_b^{2.09}} \text{ cm}^2/\text{s}$
$D_e, \ D_f$	$R_i \leq R_s: \quad \dfrac{3.42 \times 10^6 \Omega^{4/3} \, e^{-108000/RT}}{\pi R_i^2 (1.12 \times 10^{-6})^2} \text{ cm}^2/\text{s}$ $R_i > R_s: \quad \dfrac{3.42 \times 10^6 \Omega^{4/3} \, e^{-108000/RT}}{\pi R_i^2 R_s^2} \sin\left[\dfrac{0.5 \frac{R_s}{R_i}}{}\right]^2 \text{ cm}^2/\text{s}$
R_s	$1.12 \times 10^{-6} \text{ cm}$
δ	2×10^{-4}
λ	$5 \times 10^{-7} \text{ cm}$
b_o	$2 \times 10^{-17} \text{ cm}^3$
σ_b	$0.01 \text{ cm}^2/\text{cm}^3$
σ_e	0.02
γ	$1601.4 - 0.3457T \text{ ergs/cm}^3$ (solid)
γ_L	450 ergs/cm^3 (liquid)
D_u	$2.0 \, e^{-64200/T} \text{ cm}^2/\text{s}$
D_{gb}^W	$3.1 \times 10^{-8} \, e^{-24000/T} \text{ cm}^3/\text{s}$

†For nonequilibrium conditions, FASTGRASS utilizes a theoretical model for the diffusion of overpressurized fission-gas bubbles due to Rest.[6]

which is the value which makes the 2nd term on the RHS of Eq. (48) correspond to the product of the bubble density and the interaction volume swept out by each bubble.

For fuel matrix dissolution, FASTGRASS considers the interaction between two distinct bubble size populations: those that had been in the fuel lattice prior to fuel dissolution and those that had been on the grain boundaries or in a liquefied lamina. The coalescence probability for these bubbles is given by

$$P(R_1, R_2) = 2\pi(D_1 + D_2)(R_1 + R_2) + \pi(R_1 + R_2)^2(V_2 - V_1), \qquad (49)$$

where R_1, D_1, V_1 and R_2, D_2, V_2 are the radius, diffusivity, and velocity of bubble size distribution 1 and 2, repectively. Prior to fuel liquefaction/ dissolution, the bubbles are assumed to be spherical in the bulk, lenticular on the grain faces, and ellipsoidal on the grain edges. Subsequent to fuel liquefaction/dissolution, all bubbles are assumed to be spherical.

FASTGRASS analyses of the PBF-SFD 1-1 test indicate that liquefac- tion-induced fission product release depends on the initial coalescence and growth of relatively small (0.04-μm-diameter) bubbles in the liquefied material due to a volume diffusion mechanism (i.e., the fuel used in SFD 1-1 was trace-irradiated and populated with a distribution of extremely small bubbles before the onset of liquifaction/dissolution; see Fig. 2). Whereas volume diffusion (i.e., self diffusion of the U^{4+} ion) is relatively slow in solid UO_2, it appears to be a significant factor in the motion of small bubbles in liquefied UO_2. The growth of small bubbles in the liquefied material is predicted to occur mainly by the volume diffusion mechanism until the bubbles reach sufficient size (see Fig. 2). Subsequently, the release of

fission gas (and other fission products trapped in the bubbles) is dominated by the motion of relatively large bubbles (~1 μm diameter) under buoyant forces.

4. Comparison between Theory and Data

The predictions of Ba and Sr release behavior have been compared with two sets of data: (1) the data obtained by Parker and Barton[19] based on out-of-reactor induction heating experiments on declad, crushed low-burnup (1000 and 4000 MWd/t) pellets; and (2) data from the more recent in-reactor PBF-SFD Tests,[20] in which one-meter-long, trace-irradiated (89 MWd/t) and normally irradiated (35000 MWd/t) fuel rods were tested under accident conditions.

Comparison with Out-of-Reactor Data

In Table 5, the data of Parker and Barton[19] are compared with FASTGRASS predictions of Xe, Ba, and Sr release at four fuel temperatures and two values of fuel burnup. Parker and Barton[19] heated irradiated UO_2 specimens for ~5.5 h in an inert environment. Because fuel fragments having unknown values of open pore-solid surface area were used in the majority of the tests, a quantitative comparison between theory and experiment is difficult. In order to simulate the fragmented state of the test samples, 10% and 25% of the grain boundaries were assumed to be fractured for the 1000 and 4000 MWd/t samples, respectively. As is evident from Table 5, the FASTGRASS predictions follow the trend of observed Xe, Sr, and Ba release as a function of temperature and burnup. For low-burnup irradiations, most of the Ba and Sr is predicted to be in atomic form rather than in a sequestered state, and thus available for diffusional release. During the rather long time at temperature ($\approx$5.5 h), FASTGRASS predicts significant release. This prediction is borne out by the data; e.g., in the case of the 4000-MWd/t fuel fragments, the measured Ba release was $\approx$18% at 1780°C and $\approx$60% at 1980°C. The

corresponding FASTGRASS-predicted values follow the trend of these data; i.e., FASTGRASS predicted 11% and 57%, respectively. It should also be noted that the Parker and Barton[19] data show some anomalous behavior. For example, at 1000 MWd/t and 1610°C the measured Ba release is a factor of two larger than the Xe gas release. This type of reported behavior is even more pronounced for the case of I and Cs release (not shown in Table 5), where measured I and Cs releases were up to four times higher than the Xe release.

Table 5. Xe, Ba, and Sr Release Data of Parker and Barton[19],[a] Compared with FASTGRASS Predictions

Temperature	Burnup (MWd/t)	Percent Released					
		Xe		Ba		Sr	
		Data	Theory	Data	Theory	Data	Theory
1400°C	1000	0.5	0.2	1.8	0.009	0.06	0
2552°F	4000	6	2	0.5	0.002	0.08	0
1610°C	1000	6	3.5	12	1.3	0.2	0.03
2930°F	4000	14	9	15	0.5	0.5	0.02
1780°C	1000	14	12	21	9	3.7	1
3236°F	4000	42	29	18	11	6	1
1980°C	1000	49	27	51	26	10	17
3596°F	4000	71	69	60	57	33	23

[a]Fragments of irradiated fuel, weighing 0.1-0.2 g, were held at the indicated temperatures for 5.5 h.

Information on the predicted release mechanisms for these fission products is presented in Table 6. Results for Sr are similar to those of Ba. The majority of intragranular release during these low-burnup tests is predicted to occur by a grain growth/grain-boundary-sweeping mechanism. Grain growth/grain-boundary-sweeping effects are expected to be less important in higher burnup fuels, because of the increased presence of fission products on the grain boundaries, which retard boundary movement; and because of sequestering of Ba and Sr by oxygen in the fuel during fissioning.

Table 6. Predicted Intragranular Migration of Xe and Ba in 4000-MWd/t Fuel Fragments During the Parker and Barton Tests (Ref. 16)

Temp. (°C)	Product	Percent Released to Grain Boundary by	
		Diffusion	Grain Boundary Sweeping
1400	Xe	72	28
	Ba	8	92
1780	Xe	11	89
	Ba	12	88
1980	Xe	8	92
	Ba	14	86

Table 7. Predicted Chemical Form of Retained Ba (4000 MWd/t)

Temp. (°C)	Form	Percent Located on		
		Lattice	Faces	Edges
1400	Ba	0.25	0	0
	BaO(c)	5.75	0	0
	BaO(g)	0	0	0
	$BaUO_4$	94	0	0
1610	Ba	5.5	0	0.1
	BaO(c)	23	0	0.4
	BaO(g)	0	0	0
	$BaUO_4$	70	0	1
1780	Ba	22	0	7
	BaO(c)	26	0	8
	BaO(g)	0	0	0
	$BaUO_4$	28	0	9
1980	Ba	16	0	50
	BaO(c)	6	0	19
	BaO(g)	0	0	0
	$BaUO_4$	2	0	7

As is shown in Table 7, the Ba and Sr species migrating in the fuel are predicted to be primarily in atomic form (this is also valid for Cs, not shown in the table). Very little $BaO(g)$, and $SrO(g)$, and CsI are calculated to exist in bubbles, owing to the relatively low vapor pressure (e.g., as compared to the noble gases) and the limited available bubble volume for 4000 MWd/t irradiated fuel. These calculations indicate that if $BaO(g)$, $SrO(g)$, and CsI exists outside of the fuel, the molecules were formed, for the most part, either in the fuel open porosity or at the fuel surface, and not within fission gas bubbles.

Comparison with In-Reactor Data

The PBF-SFD test series[10] was initiated to obtain data on fission product behavior under conditions of severe core degradation similar to those experienced at TMI-2. Each test was performed with one-meter-long Zircaloy-clad UO_2 fuel rods arranged in a 6x6 array, with corner rods missing. Trace-irradiated fuel ($\approx$90 MWd/t) was used in the first and second tests, and normally irradiated fuel ($\approx$30,000 Md/e) was used in the last two tests. The high-temperature fuel destruction phase of each test was achieved by reducing coolant inlet flow to the test bundle and increasing the reactor power; the results were coolant boiloff, clad ballooning and rupture, Zircaloy and fuel oxidation by steam, clad melting and relocation, and release of noble gases and VFPs from the severely damaged fuel rods. Additional details of the test design and conduct can be found in Refs. 10, 17, and 20.

Test data for the PBF-SFD 1-1 and 1-4 tests are presented in Table 8. The SFD 1-1 transient consisted of a slow heat-up of trace-irradiated (89 MWd/t) fuel to ~1600 K, followed by a rapid heating that was driven by cladding oxidation in the upper regions of the fuel bundle. The peak fuel temperatures in most of the fuel rods were $\geq$2650 K. A significant amount of

Table 8. Percentage Fission Product Release Measured During Two PBF-SFD Tests, Compared with FASTGRASS Predictions

| Species | SFD 1-1 | | | SFD 1-4 | | |
| | | Theory | | | Theory | |
	Data	Total Release	Liquefaction Release	Data[a]	Total Release	Liquefaction Release
Noble Gas	6.0±3.0	4.4	3.9	30-51	42	15
I	12	4.6	4.0	24	42	15
Cs	9.4	4.9	4.3	42	35	12.5
Te	≈0.3	0.15	0.13	<0.5	0.3	0.1
Ba	≈0.5	0.9	0.8		12	4
Sr	--	0.3	0.25		14	5

[a]Excluding irreversible deposition and filter content.

liquefaction/dissolution occurred in the SFD 1-1 test. In the SFD 1-4 test, the transient closely matched that of SFD 1-1; however, irradiated (~35,000 MWd/t) fuel rods were used in the SFD 1-4 test bundle. The liquefaction/dissolution scenario for SFD 1-4 was assumed to be identical with that of SFD 1-1 test.

The spatial and axial temperature profiles provided to FASTGRASS were derived from the SCDAP computer model[21] calculations and were adjusted to the best-estimate temperature profile. The initial effective grain size was 8 μm. The general lack of fuel oxidation during the SFD 1-1 test dictated a grain growth model driven only by temperature. The 17% fuel dissolution noted during post-irradiation examination was simulated in FASTGRASS by allowing one of the ten fuel nodes to go into total dissolution (monotectic melting temperature = 2650 K), while four of the remaining nodes were modeled to have grain boundary liquefaction (liquefaction temperature = 2150 K). Since relocation information was not supplied, the cylindrical fuel geometry was maintained by FASTGRASS throughout the simulated transient.

In Fig. 4, the FASTGRASS-predicted fission gas release rate for the SFD 1-1 test is compared with measured release rates. FASTGRASS calculations are shown with and without the effects of fuel liquefaction/dissolution. The release rates predicted by FASTGRASS with the effects of liquefaction/dissolution agree quite well with the trend of the SFD 1-1 measured release rates. In Figure 5 and Table 8, the FASTGRASS noble gas release fractions are compared with the results of the on-line and grab-sample measurements. The results for FASTGRASS made with the effects of liquefaction/dissolution predict releases in better agreement with the measurements.

The calculated SFD 1-1 fractional noble gas release (Fig. 5) is about 4.4%, with liquefaction occurring at about 2000 s. As indicated in Table 8, about 3.9% noble gas release is predicted from nodes that experience liquefaction, the remainder (0.5%) being released during solid phase fuel heatup. Although an enhanced release is noted for liquefied fuel over that from the solid matrix, the release is still relatively low (4.4% total) since the bubble size for trace-irradiated fuel is quite small ($\approx$10 Å diameter), and the mobility of bubbles in liquids increases with increasing size.

Figure 6 shows GRASS-SST[6] and FASTGRASS calculations of the bubble-size distribution in liquified UO_2 just subsequent to fuel dissolution for SFD 1-1 and SFD 1-4. (FASTGRASS considers two bubble size classes for fuel which has undergone dissolution, corresponding to bubbles which existed within the bulk and on the grain boundaries just prior to the phase change.) Also shown in Fig. 6 are the calculated results for SFD 1-1 just after fuel resolidification. For the trace-irradiated SFD 1-1 fuel, the more detailed GRASS-SST mechanistic model calculates the peak in the bubble size distribution in liquid fuel occurring at a bubble diameter of ~0.015 μm. For
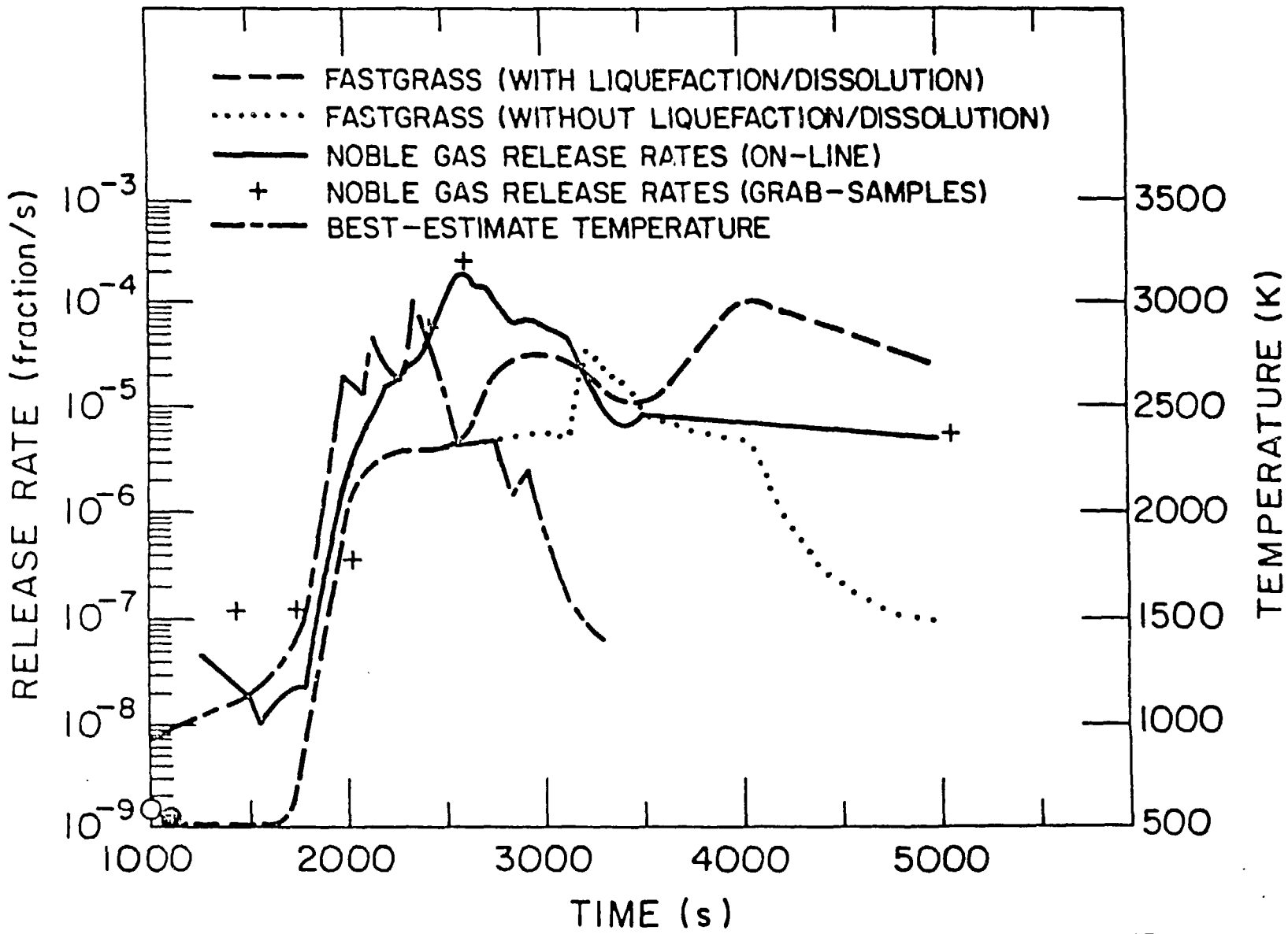
Figure 4. FASTGRASS-Calculated Fission Gas Release Rates for SFD 1-1, With and Without the Effects of liquefaction/Dissolution. Compared With Measured Data.
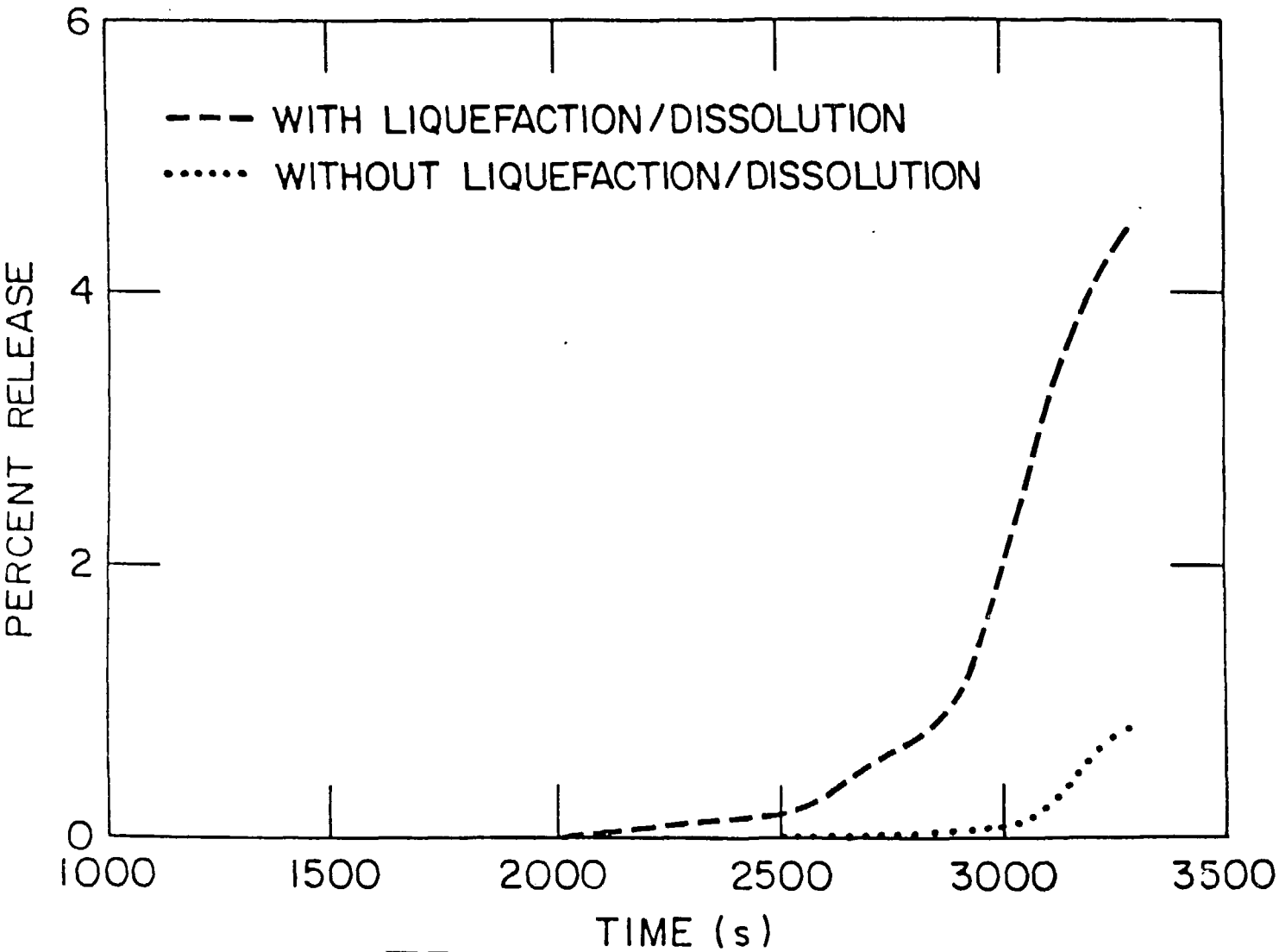
42

Figure 5. FASTGRASS-Calculated Percent Noble Gas Release for SFD 1-1 With and Without the Effects of Fuel Liquefaction/Dissolution.

The figure shows a plot of PERCENT RELEASE (y-axis, 0 to 6) versus TIME (s) (x-axis, 1000 to 3500). Two curves are shown:
- WITH LIQUEFACTION/DISSOLUTION (dashed line)
- WITHOUT LIQUEFACTION/DISSOLUTION (dotted line)

the irradiated fuel of SFD 1-4, GRASS-SST calculates a bubble-size distribution in liquid fuel with the peak occurring at a bubble diameter of ~0.06 μm. The calculated bubble-size distribution for SFD 1-4 is both higher and broader than that for SFD 1-1. Thus, as the bubble velocity in the liquified fuel depends on bubble size (e.g., see Fig. 2), and the bubble coalescence rate depends additionally on bubble density [e.g., see Eq. (48)], gas bubble escape from liquified fuel (and, thus the escape of other fission products which are swept out by the bubbles, e.g., I and Cs) will, in general, be much greater for normally irradiated fuel than for low burnup fuel. Figure 6 also shows that FASTGRASS tends to approximate the GRASS-SST bubble-size distributions (at least at the onset of dissolution) by calculating a high density of smaller than "average" size bubbles (i.e., the peak of the distribution), and a low density of larger than "average" size bubbles.

As the system evolves in the liquified state, the FASTGRASS-calculated bubble sizes come into better agreement with those calculated by GRASS-SST. This is shown in Fig. 6 by the GRASS-SST calculated bubble-size distribution for SFD 1-1 just subsequent to fuel resolidification, and the corresponding FASTGRASS calculated value. The predicted releases are on the order of 50%. The results for SFD 1-4 do not appear in Fig. 6 because the predicted releases approached 100%. These results demonstrate that in low burnup fuel (e.g., SFD 1-1, TMI-2), appreciable fission-product retention in previously molten fuel is possible.

The curves shown in Figures 4 and 5 incorporate the FASTGRASS grain-growth-fission-product-sweeping model. In view of the postirradiation examination findings of little fuel oxidation, the FASTGRASS simulation of the SFD 1-1 test incorporated grain growth kinetics which were activated solely by temperature. The initial grain size was taken as 8 μm, and the end-of-test
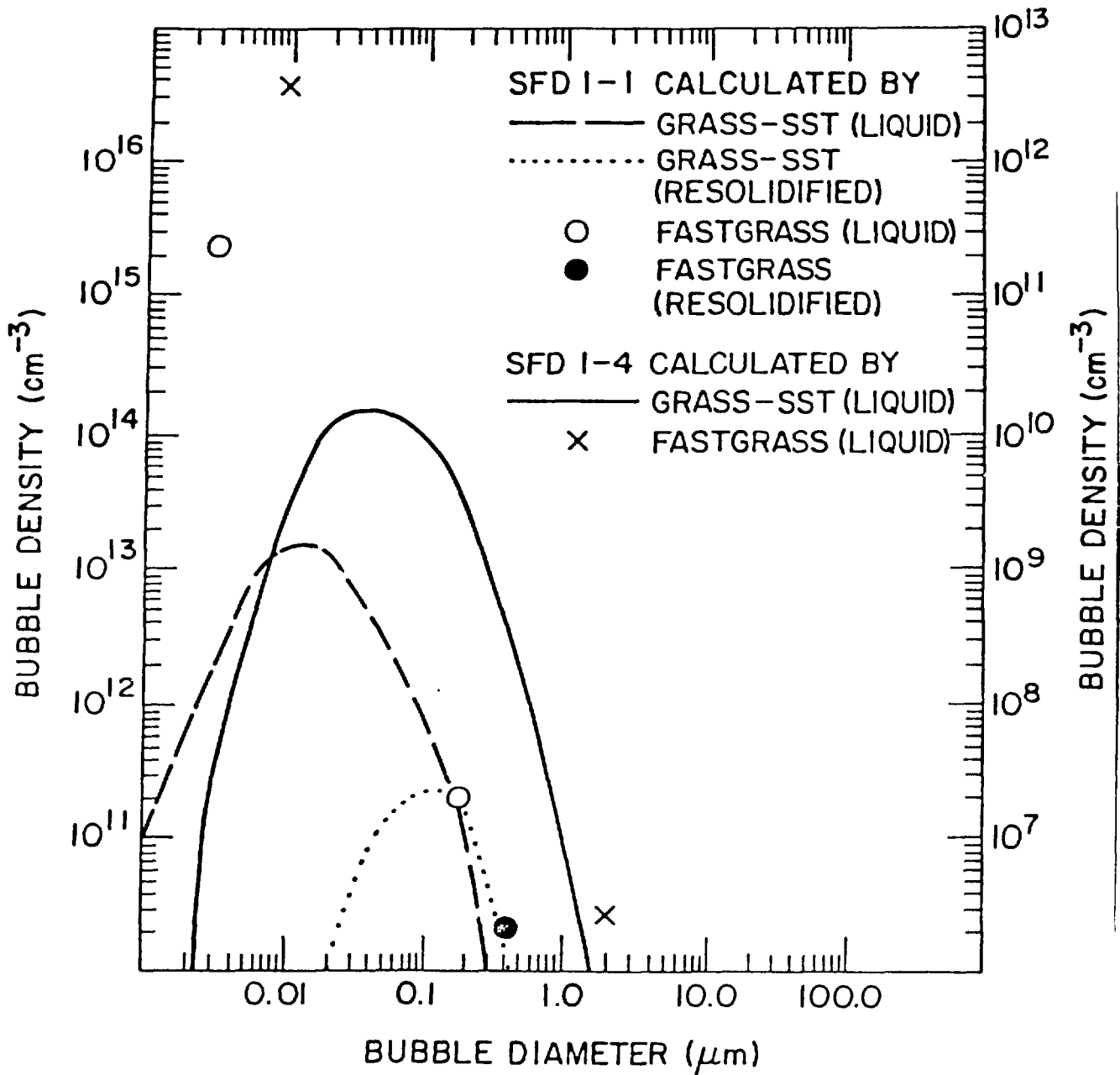
Figure 6. GRASS-SST- and FASTGRASS-Calculated Bubble-Size Distribution in Liquefied Fuel Just Subsequent to Fuel Dissolution for SFD 1-1 and SFD 1-4. Also shown are the caluclated results for SFD 1-1 just subsequent to fuel resolidification.

calculated grain size was ~12 μm. This compares favorably with the 10-12 μm grain size found from PIE of fuel debris samples. Although only limited grain growth is estimated by FASTGRASS, the effect of such grain growth on the sweeping of fission gas from the grain interior to grain boundaries during solid-phase fuel heatup is pronounced. As shown in Table 9, FASTGRASS predicts that from 3% to 85% of the retained gas in the undissolved pellets is trapped on the grain boundaries during solid-phase fuel heatup. However, once liquefaction temperatures (2150 K) are reached, partial release of this previously entrapped gas inventory is predicted to commence, with release occurring over the slow cooldown period, when the liquefied fuel was slowly cooled to a resolidified debris mass. Subsequent microcracking of fuel upon cooldown termination provides an additional mechanism (not considered here) for added fission product release that was noted late in the test.

Table 8 also shows a comparison of release fractions measured during the SFD 1-1 and 1-4 tests and the FASTGRASS VFP/AEFP-calculated release fractions. As indicated, the FASTGRASS predictions are in reasonable agreement with the reported data. However, as the SFD 1-1 and 1-4 temperature and liquefaction/dissolution scenarios are somewhat uncertain, these results should again be considered qualitative rather than quantitative. For the trace-irradiated fuel of the PBF-SFD 1-1 test, low release is predicted (Table 8). Approximately 1% of the Ba and 0.3% of the Sr are predicted to migrate to grain boundaries and to trapped there during solid-phase fuel heat-up. During fuel liquefaction/dissolution, this inventory of Ba and Sr is predicted to be released. This prediction agrees well with the test data (<1% measured release). Reliable data on Ba and Sr release for the SFD 1-4 test are not available at this time.

Also shown in Table 8 is the quantity of fission products predicted to be released through the liquefied regions of the fuel after fuel heat-up and

Table 9. FASTGRASS-calculated I, Cs, and Xe Morphology for Test SFD 1-1

Axial Node	Maximum Temperature	Percent of Fission Product Inventory Trapped on Grain Boundaries						
		Fuel Liquefaction/Dissolution	Xe	I	Cs	CsI	Cs_2UO_4	Cs_2MoO_4
1[a]	2349	Yes	17.6	21.8	26	0	0	0
2[b]	3025	Yes	--	--	--	--	--	--
3	2862	No	85.4	86.8	20.3	0	63.7	0
4	2662	No	69	72.6	9.2	0	61.8	0
5	2663	No	78.3	80.1	22.9	0	54.8	0
6[a]	2438	Yes	17	18.8	19.1	0	1.32	0
7[a]	2437	Yes	29.8	28.3	5.8	0	26	0
8[a]	2436	Yes	29.4	26.9	1.6	0	29.1	0
9	2439	No	35	32.5	2.0	0	21	0
10	2213	No	3.3	13.1	15.4	0	1.2	0

[a]Grain boundary liquefaction temperature = 2150 K.
[b]Monotectic melting temperature = 2650 K.

during fuel cooldown. For the SFD 1-1 test, essentially all of the fission products are predicted to be released during the slow cooldown of liquefied fuel to a reconfigured solid debris mass. The reason for this result is that during solid-phase heatup, in trace-irradiated fuel, very little open porosity is calculated to exist on the grain boundaries. Thus, fuel liquefaction provides release paths for the entrapped fission products. In the higher burnup SFD 1-4 fuel, fission product release is partitioned between liquefaction release and release through networks of open porosity. The higher degree of open porosity in the irradiated SFD 1-4 fuel is due to much higher concentrations of fission gas on the grain boundaries, and thus more extensive interlinkage to the fuel surface.

Table 9 presents the FASTGRASS-calculated I and Cs behavior for SFD 1-1. The salient feature to note is that the fission product I shows the same release characteristics as Xe and that no CsI formation is predicted. Iodine is predicted to remain in atomic form and diffuse through the fuel matrix similarly to Xe. This observation is also supported by the work reported in Refs. 17 and 18. On the other hand, fission product Cs either reacts with the fuel to form Cs uranate or migrates in atomic form. Since both I and molybdenum (Mo) are fission products and are widely dispersed in the fuel matrix for trace-irradiated conditions, essentially no formation of CsI and $CsMoO_4$ is predicted for the SFD 1-1 fuel.

Table 10 presents the FASTGRASS-calculated release characteristics of Sr and Ba for the SFD 1-1 conditions. Both Sr and Ba react with the fuel or with oxygen freed from the fissioning UO_2 to form BaO, $BaUO_4$, and SrO. The chemical affinity of Ba and Sr for oxygen results in near-total sequestering of Sr and Ba as oxides or uranates within the fuel matrix or at grain boundaries and at the fuel open porosity.

Table 10. FASTGRASS-calculated Ba and Sr Morphology for Test SFD 1-1

Axial Node	Maximum Temp. (K)	Percent of Fission Product Inventory Fuel Liquefaction/Dissolution	Trapped at Grain Boundaries (%)				
			Ba	BaO	BaUO$_4$	Sr	SrO
1[a]	2349	Yes	0.14	1.9	14	0	12.6
2[b]	3025	Yes	--	--	--	--	--
3	2862	No	0	0.9	82	0	82.2
4	2662	No	0	0.4	67.3	0	64.9
5	2663	No	0	0.9	76.4	0	75.3
6[a]	2438	Yes	0	0.7	29.7	0	25.9
7[a]	2437	Yes	0	0.1	23.7	0	18.4
8[a]	2436	Yes	0	0.5	18.3	0	13.8
9	2439	No	0	0.25	21.5	0	17.6
10	2213	No	0	0.09	3	0	1.7

[a]Grain boundary liquefaction temperature = 2150 K.
[b]Monotectic melting temperature = 2650 K.

5. COMPARISON OF FASTGRASS WITH CORSOR

Out-of-reactor fission product release and aerosol behavior tests on severely damaged fuel are being conducted at ORNL. In these tests, samples of previously irradiated fuel (10,000 to 30,000 MWd/t) are induction heated in a flowing steam environment with cladding temperatures simulating a decay heat/loss-of-coolant accident. Several experiments have been conducted to date; the most pertinent to the present discussion is the HI-3 test, where post-test examination indicated no evidence of fuel liquefaction, and the HI-4 test where significant liquefaction occurred.[22]

Figure 7 shows FASTGRASS predictions of fission gas release for the ORNL HI-3 test, with and without the effects of fuel liquefaction, compared with the test observations. The fuel specimen for HI-3 consisted of a 20.3-cm-long fuel segment from a rod which had been irradiated in the H. B. Robinson Reactor to about 30,000 MWd/t. The FASTGRASS calculations made with the
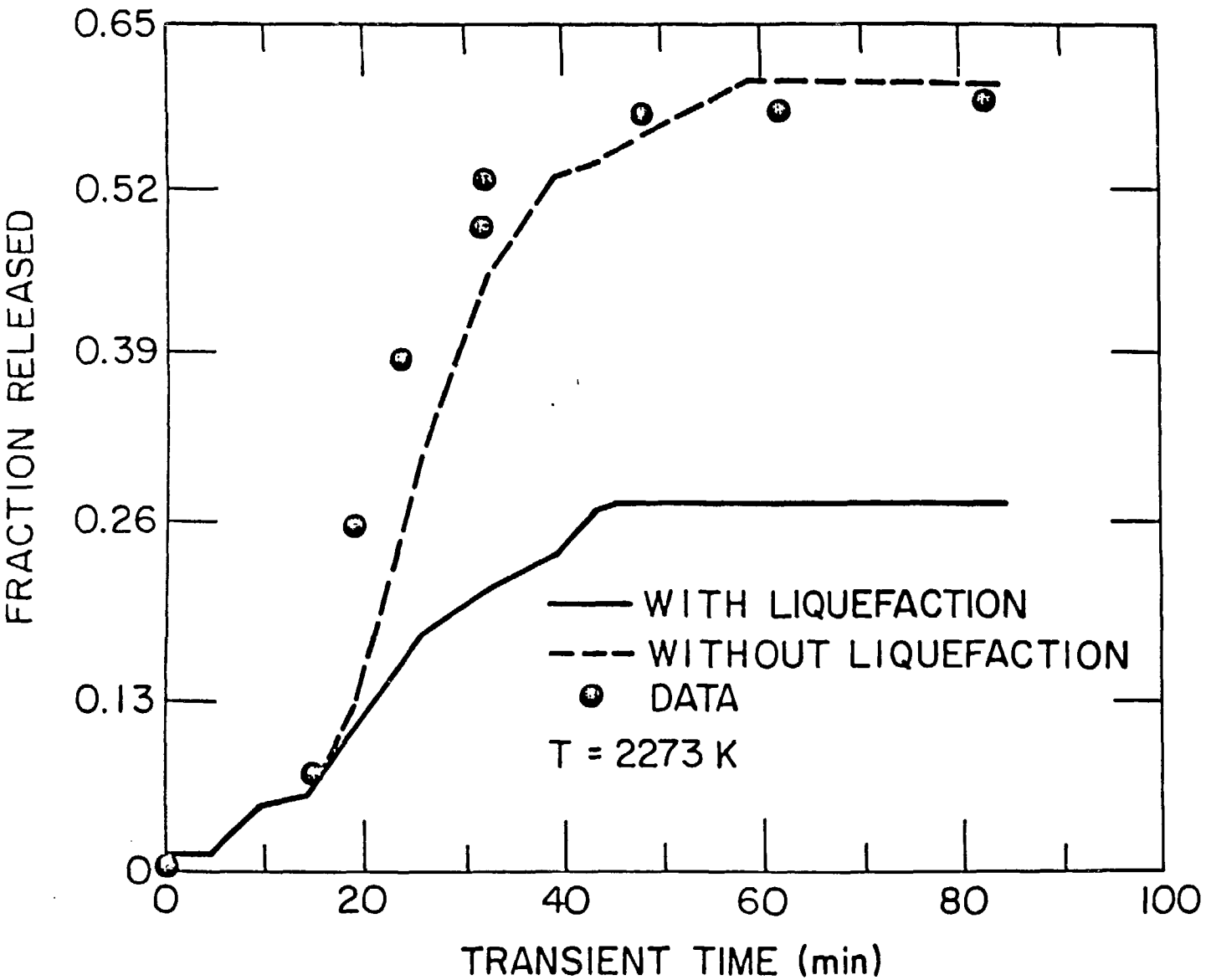
Figure 7. FASTGRASS Predictions of Fission Gas Release During ORNL Test HI-3 (Max. Fuel Temperature = 2273 K), With and Without the Effects of Fuel Liquefaction, Compared With Measured Values.

assumption of no liquefaction are in good agreement with the data. The calculations, made with the assumption that fuel liquefaction occurred in test HI-3 (which was not the case), show a degradation in the fission gas release and are not in agreement with the data. The reason for this result is that for the fuel liquefaction condition, the enhanced growth of fission gas bubbles in the liquefied lamina bordering the UO_2 grains reduces grain growth rates and reduces sweeping of intragranular fission products into the liquefied region. In addition, just subsequent to fuel liquefaction, fission product release rates are reduced owing to decreased mobility in a viscous medium as compared to vapor transport through interconnected tunnels.

The effect of reduced grain growth rates during fuel liquefaction is demonstrated in Fig. 8, which shows FASTGRASS predictions for grain growth during test HI-3 with and without the effects of fuel liquefaction. Also shown in Fig. 8 is the grain size observed in the post-tested fuel.[23] The grain size prediction obtained without the effects of fuel liquefaction is consistent with the observations. The FASTGRASS results for fission gas release and grain growth during test HI-3 in the absence of any fuel liquefaction are consistent with the fact that no evidence of any fuel liquefaction was observed in test HI-3.

Figure 9 shows FASTGRASS predictions for fission gas release during test HI-4 with and without the effects of fuel liquefaction, compared to the experimental observations. The fuel specimen for ORNL test HI-4 consisted of a 20.3-cm-long fuel segment from a rod that had been irradiated in the Peach Bottom-2 reactor to about 10,100 MWd/t.

Grain boundary liquefaction of the fuel, i.e., formation of liquid uranium at temperature, was observed in portions of the fuel, principally near large amounts of Zircaloy.[22] As shown in Fig. 9, the FASTGRASS results for
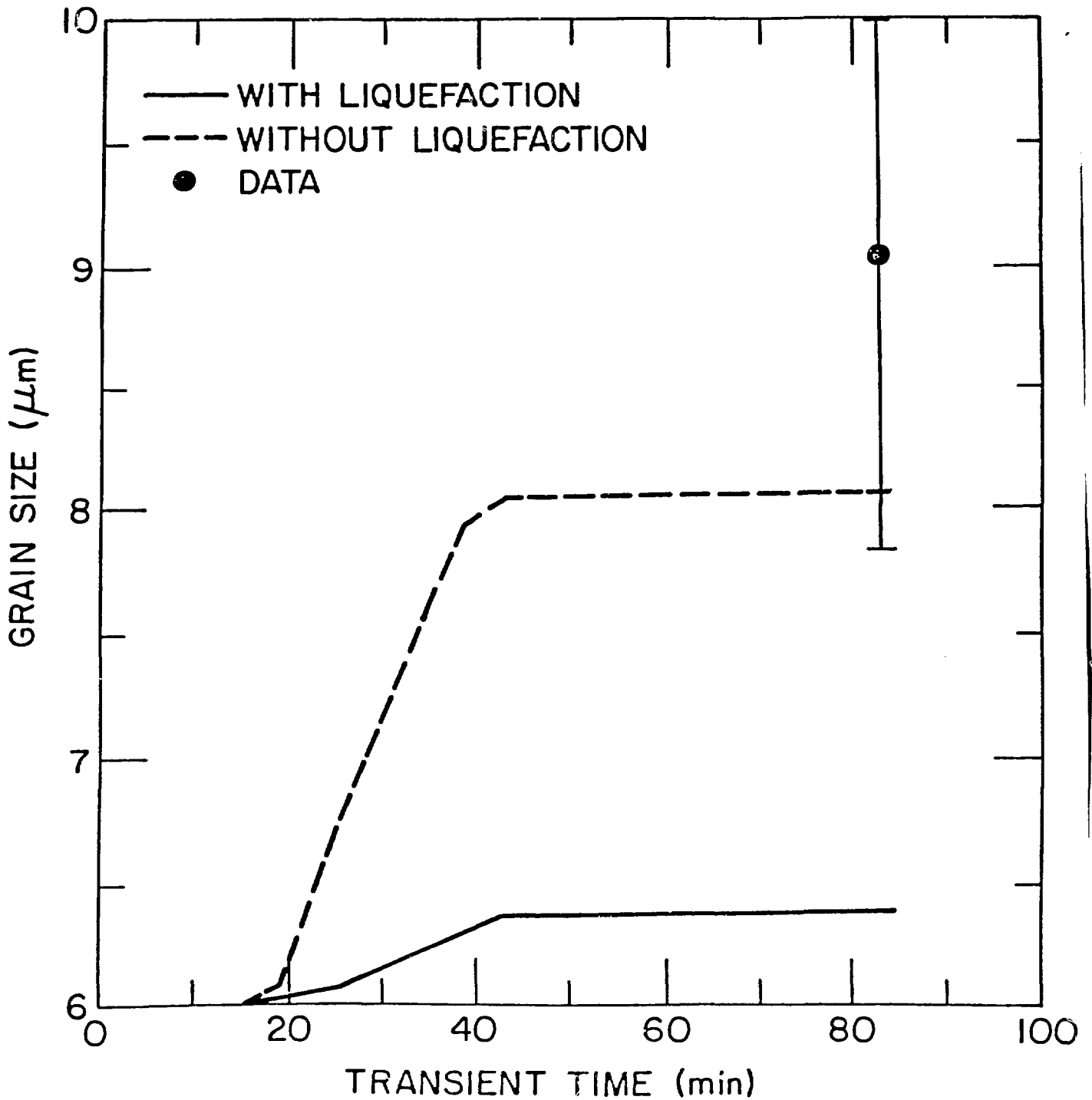
Figure 8.   FASTGRASS Predictions of Grain Growth During ORNL Test HI-3, With and Without the Effects of Fuel Liquefaction, Compared With Measured Values.
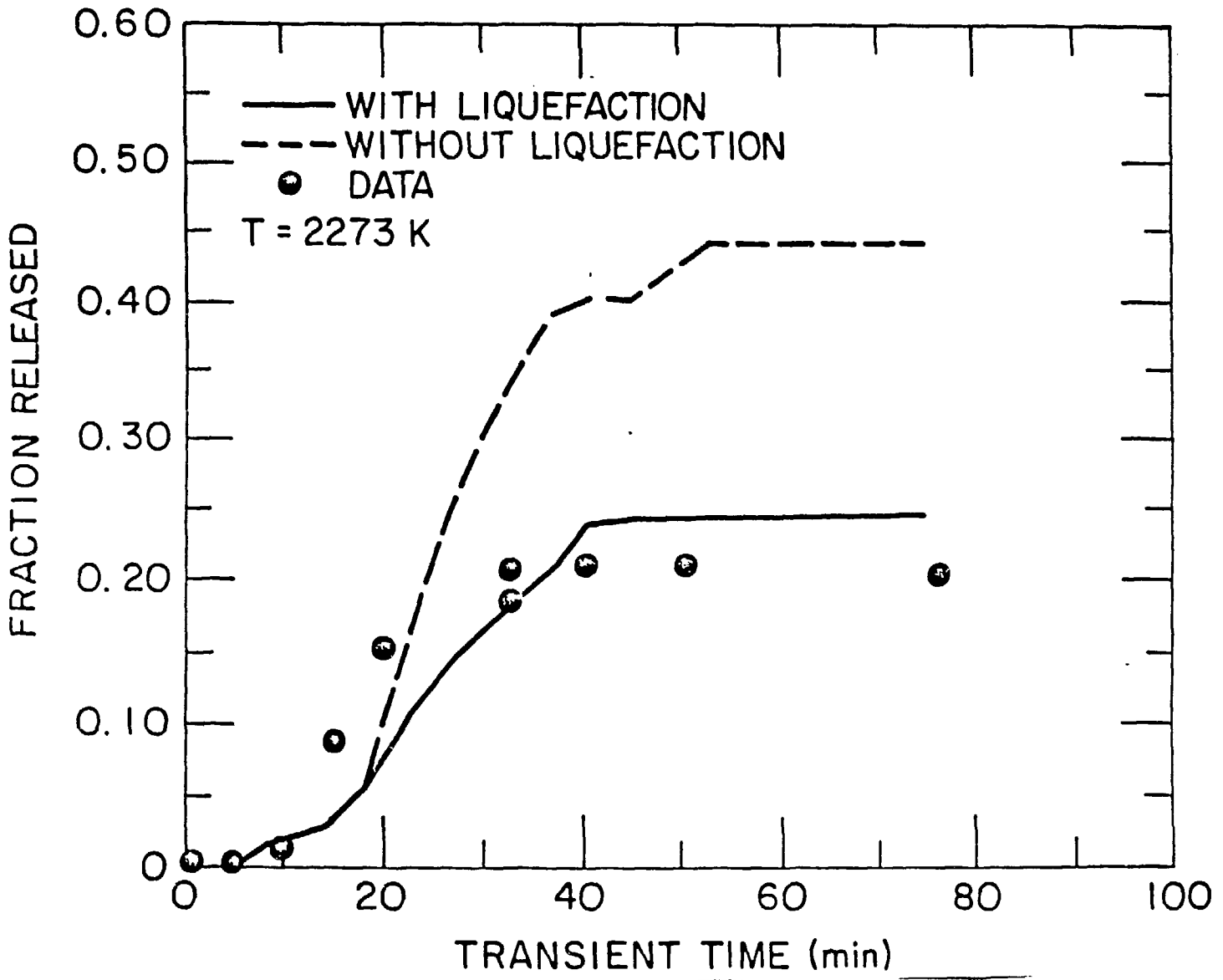
Figure 9. FASTGRASS Predictions of Fission Gas Release During ORNL Test HI-4 (Max. Fuel Temperature = 2273 K), With and Without the Effects of Fuel Liquefaction, Compared with Measured Values.

fission gas release during test HI-4 under liquefaction conditions are consistent with this observation. The calculations made with the assumption of no fuel liquefaction effects (dashed line) substantially overpredict the reported data. In addition, the FASTGRASS prediction of less than 10% increase in grain size is consistent with the observation of no grain growth within a 15% uncertainty range.[23]

The NUREG-0772[24] fission product release correlations (sometimes referred to as the CORSOR correlations) assume, for molten fuel, 100% instantaneous release of noble gases and the volatiles I and Cs; in contrast, release of these fission products from solid fuel is predicted to occur within about 10 min. at temperatures exceeding ≈2000°C (2273 K). However, the PBF-SFD data indicate that substantial fission product retention in liquefied fuel can occur. FASTGRASS analysis of these test data supports these observations (see Section 4). For the trace-irradiated SFD 1-1 fuel, the low concentration of fission products in the fuel matrix is predicted to have prevented appreciable bubble nucleation and growth, and hence, appreciable bubble escape velocities (see Figs. 1, 2, and 6). For higher burnup fuels, the amount of release, although in general much greater than from trace-irradiated material, is still dependent on bubble mobility behavior, the fuel geometry, and the time at fuel liquefaction temperatures.

Figures 10-12 show results of FASTGRASS predictions of noble gas, Cs, and Ba integral release fractions for fuel irradiation to a 3 atom % burnup condition and the following heating/cooldown scenario:

    a.   Pre-irradiation to 3 atom percent burnup at a temperature of 1500 K (simulated normal reactor power operation).

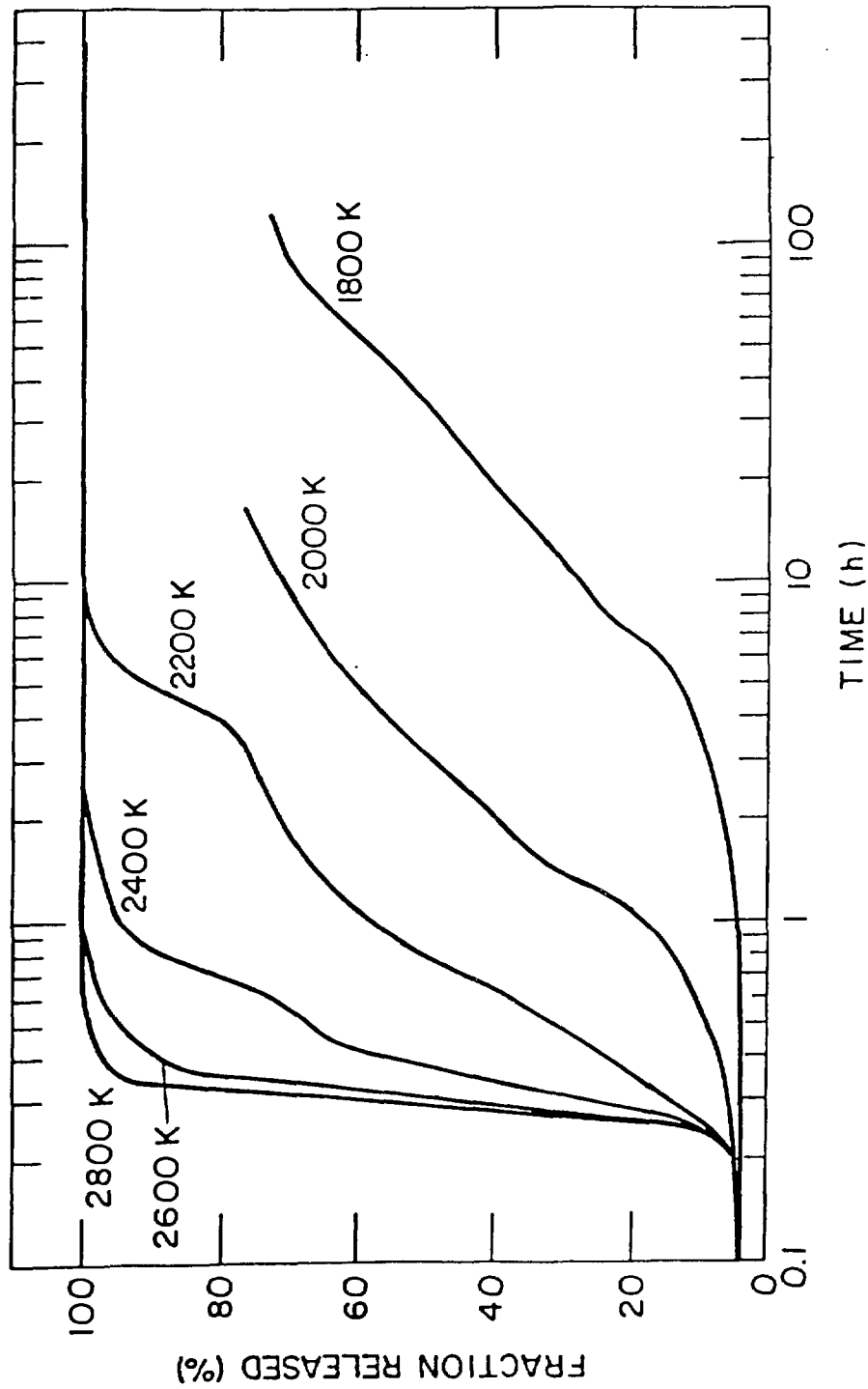   b.   Cooldown to 500 K (simulated reactor shutdown).

Figure 10. FASTGRASS-Calculated Fission Gas Release During Fuel Heatups to
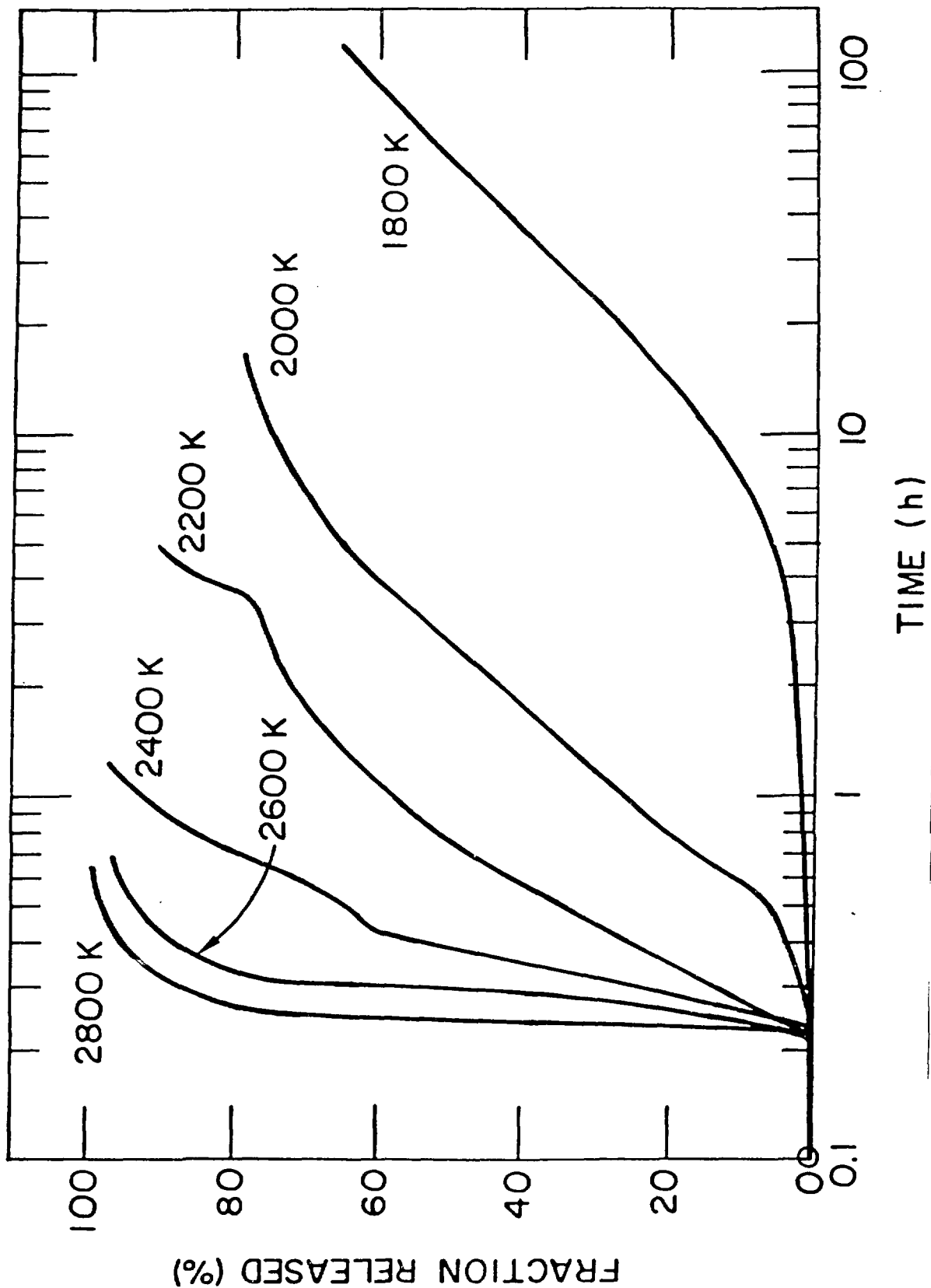1800-2800 K and During Subsequent Hold Periods.

Figure 11. FASTGRASS-Calculated Cesium Release During Fuel Heatups to 1800-
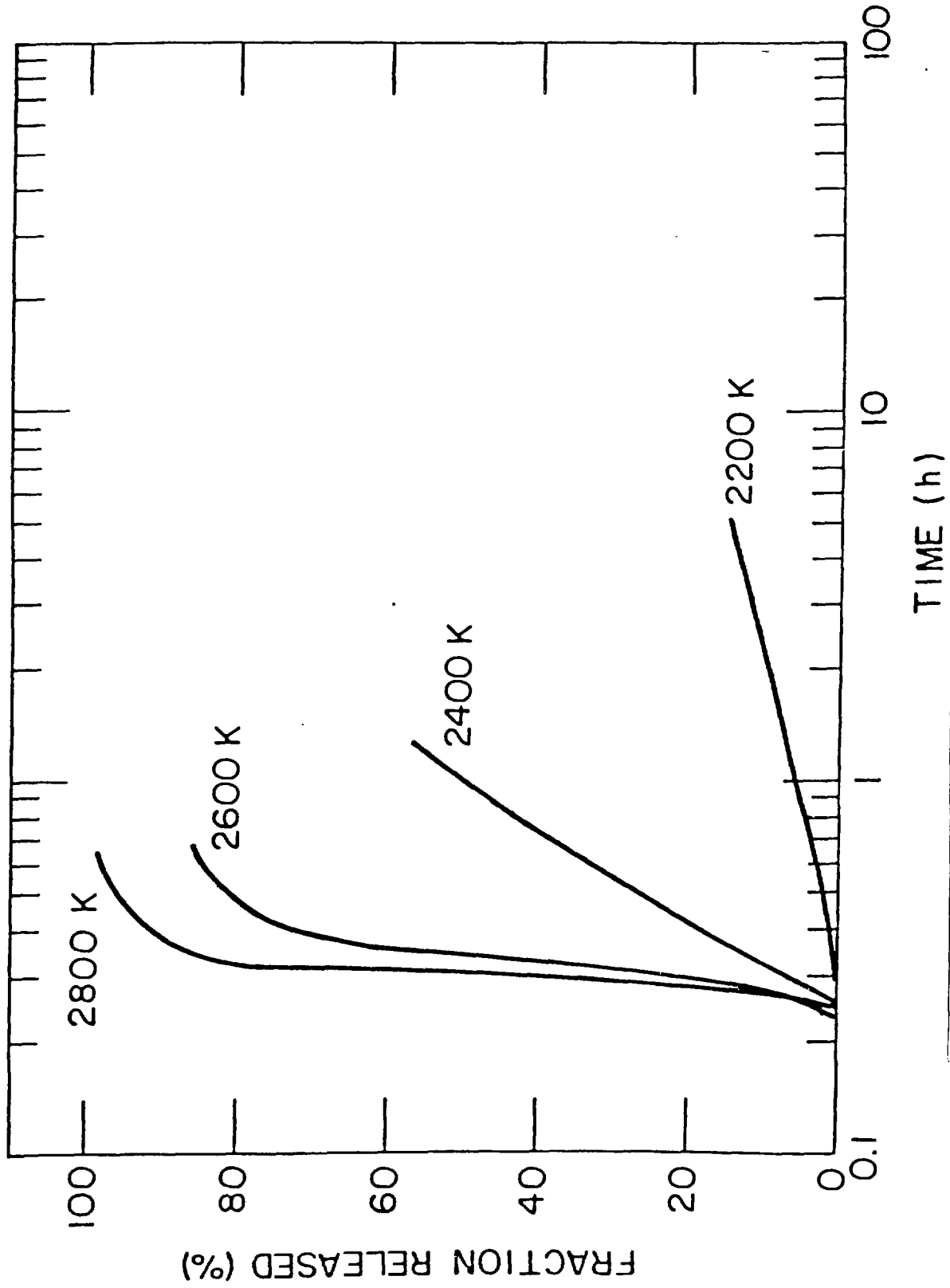2800 K and During Subsequent Hold Periods.

Figure 12.   FASTGRASS-Calculated Ba Release During Fuel Heatups to 2200-2800 K and During Subsequent Hold Periods.

c. Simulated decay heat/loss-of-coolant accident, with a heat-up rate of 2 K/s to temperatures in the 1800-2800 K range, with the fuel then held at constant temperature for up to several hundred hours.

This heating scenario is similar to that used at ORNL for the HI test series (however, the HI test hold times were ≈30 minutes). Figure 10 shows the FASTGRASS-predicted fractional release for Xe. One hundred percent fission gas release from solid fuel is predicted by FASTGRASS after an ≈11-min. hold at 2800 K (fuel heat-up took ≈19 min.), whereas hold period of a ≈10-h is required at 2200 K to produce the same 100% fission gas releases. The effect is even more dramatic at lower temperatures. The NUREG-0772[24] correlations predict 100% release at 2800 K and 2200 K in about 1 min. and 10 min., respectively. The FASTGRASS mechanistic code thus predicts a much slower release rate then the NUREG-0772 correlation, even for normally irradiated fuel (30,000 MWd/t).

Figure 11 shows similar results for Cs release. For fuel temperatures of 2000-2800 K, the Cs release is similar to the Xe release. For lower temperatures (1800 K), the Cs release is somewhat lower than the Xe release. At lower fuel temperatures the Cs tends to become sequestered in the fuel as Cs_2UO_4 and Cs_2MoO_4, although, even in the absence of such chemical effects, the FASTGRASS model for atomic Cs release carried by bubble transport would predict lower release rates than the NUREG-0772 correlation.

Figure 12 shows FASTGRASS-calculated results for Ba. Virtually no release (i.e., <1%) occurs for fuel temperatures below 2000 K and hold times of several hundred hours. At 2200 K, the calculated Ba release is as follows: 14% after ≈4 hours, 57% after a hold of ≈1-hour at 2400 K (fuel heat-up took ≈16 min.), and 98% after a hold of ≈21-min. at 2800 K. The limited release of Ba at temperatures below 2200 K is due to extensive
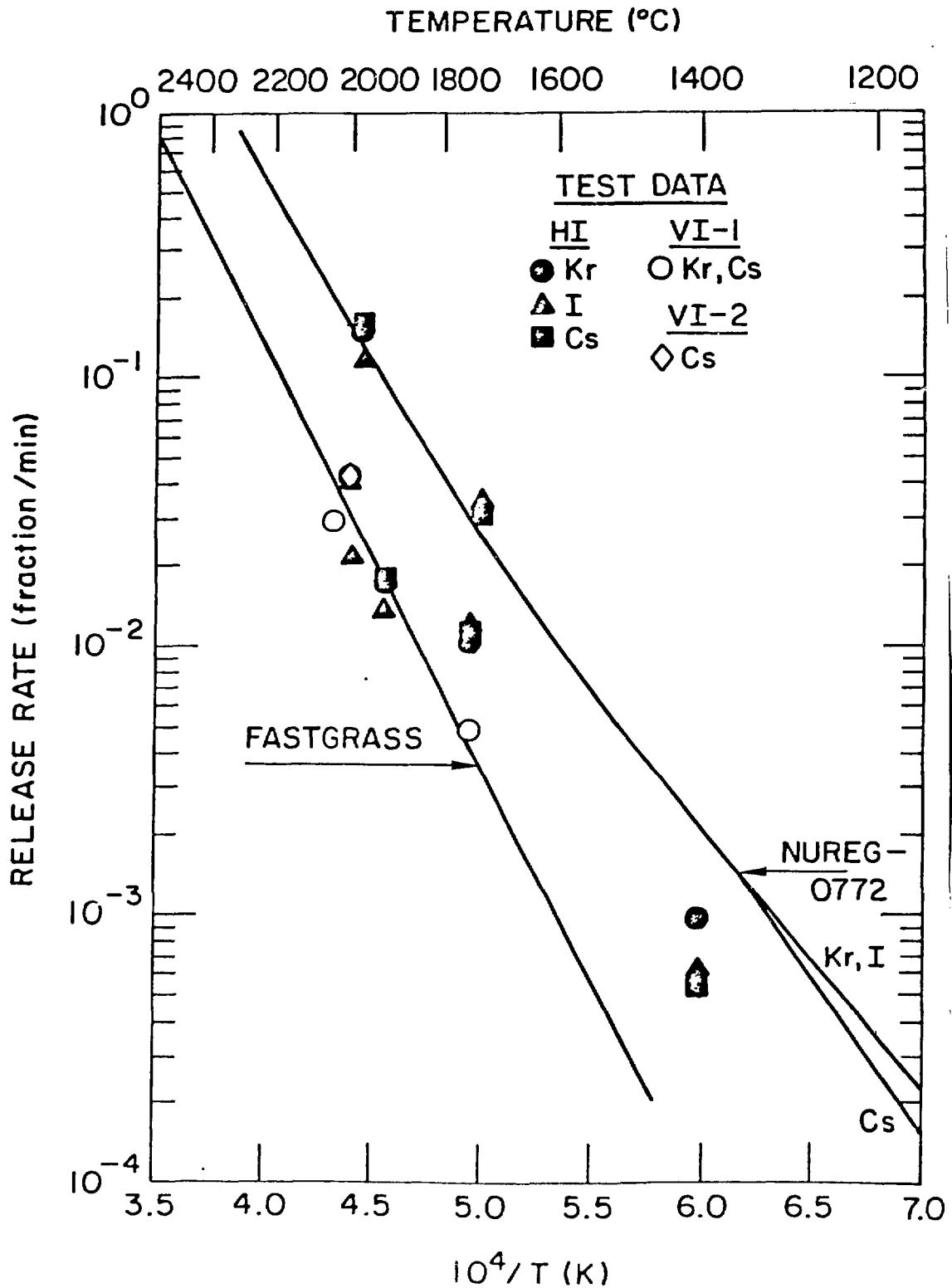
Figure 13. FASTGRASS-Calculated Release Rates From Solid Fuel Obtained From the Fractional Release Curves Shown in Figure 10 Compared With Various ORNL Data and the NUREG 0772 Release Rate Correlation.

sequestering of Ba as BaO(c) and $BaUO_4$(c) within the fuel matrix for this normally irradiated fuel.

Figure 13 presents FASTGRASS-calculated average fission gas release rates (obtained from the linear portion of the fractional release curves shown in Fig. 10), plotted against the reciprocal of the absolute temperature and compared with various ORNL data and the NUREG-0772 release rate curve.[24] The linear fit to the ORNL release data from <u>horizontally</u> tested (HI) rods results in a curve that lies between the somewhat high NUREG-0772 correlations and the FASTGRASS predictions. It should be noted that the series of points above 10^{-1} fraction/min (at 4.5 x 10^4/T) are from test HI-6, which was a short-time test (~1 min.), and the series of points at about 3.5 x 10^{-2} fraction/min (at ~5.0 x 10^4/T) are from test HI-2, which most likely experienced fuel oxidation.[23] These points should be excluded from comparison with the FASTGRASS curve, as this curve represents release from stiochiometric, solid fuel only, and for hold times representative of the linear portion of the fractional release curves shown in Fig. 10. The ORNL noble gas release data from <u>vertically</u> tested (VI) fuel rods closely mirror the FASTGRASS curve. These findings support a mechanistic approach to modeling fission product release, rather than the temperature-only empirical correlation employed in NUREG-0772.

6. CONCLUSIONS

The FASTGRASS analyses discussed in this paper underline three major conclusions about fission product behavior during severe fuel damage conditions:

1. Fission product behavior in solid fuel is strongly dependent on fuel microstructure and irradiation history as well as fuel temperatures. This conclusion is most clearly demonstrated by the

differences in fission product behavior between trace-irradiated fuel
(SFD 1-1) and irradiated fuel (SFD 1-4, ORNL tests).

2. Fission product behavior is strongly dependent on fission-product/
fuel chemistry. This conclusion is evident in the differences in
behavior between Xe, I, Cs, Ba, and Sr. Cs, Ba, and Sr become
sequestered within the UO_2 as oxides, uranates, or molybdates.
$BaO(g)$, $SrO(g)$, and CsI formation within the fuel is severely limited
by their relatively low vapor pressures and the available bubble
volume. The behavior of Cs, Ba, and Sr is strongly dependent on the
oxygen partial pressure in the fuel. The chemical form of retained
fission products is important for accidents where reheating and re
liquefaction of the fuel debris occurs after the primary accident
scenario.

3. Fuel liquefaction/dissolution, fracturing, oxidation, and relocation
strongly affect fission product behavior during severe fuel damage
types of accidents. Fuel liquefaction/dissolution provides rapid
escape paths for fission products entrapped in previously solid
irradiated fuel (in trace-irradiated fuel, liquefaction/dissolution
provides the major release paths). In addition, liquified fuel
provides a mechanism for continued high release as fuel is slowly
resolidified during the cooldown phase of the accident. The fission
product release is strongly dependent on the timing and extent of
fuel dissolution and relocation. For trace-irradiated, or very low
burnup fuel appreciable fission product retention in previously
liquified fuel can occur due to the low concentrations
of fission products, and the limited growth of bubbles in the
liquified material. For higher burnup fuel (under similar accident

conditions), much larger bubble growth is predicted, and hence, relatively lower fission product retention is expected. In addition to liquifaction effects, oxidation of solid fuel leads to enhanced diffusivities and enhanced release rates. Fuel fracturing can also provide escape paths for fission products trapped on the grain boundaries of solid fuel.

4. The FASTGRASS mechanistic approach to the prediction of fission product release during severe core damage accidents compares well with release trends noted from recent in- and out-of-reactor experiments. The FASTGRASS predictions are in much better agreement with the data over a wide range of temperature, fuel burnup, and fuel damage conditions than the present NUREG-0772 temperature-only empirical correlations.

REFERENCES

1. S. Levine et al., <u>Source Terms: An Investigation of Uncertainties, Magnitudes, and Recommendations for Research</u>, ALO-1008/NUS-3808 (March 1982).

2. J. Rest, J. Nucl. Mater. <u>120</u> (1984) 195.

3. J. Rest, J. Nucl. Mater. <u>131</u> (1985) 291.

4. J. Rest, <u>Advances in Ceramics</u>, <u>17</u> (1986) 223.

5. J. R. Matthews and M. H. Wood, Nucl. Eng. Des. <u>56</u> (1980) 439.

6. J. Rest, <u>GRASS-SST: A Comprehensive Mechanistic Model for the Prediction of Fission-Gas Behavior in UO_2-Base Fuels during Steady-State and Transient Conditions</u>, ANL-78-53 (June 1978).

7. E. E. Gruber, <u>The Role of Bubble-Size Equilibration in the Transient Behavior of Fission Gas</u>, ANL-78-36 (April 1978).

8. M. V. Speight and W. Beere, Met. Sci., <u>9</u> (1975) 190.

9. M. F. Osborne et al., in: <u>Proc. Int. Mtg. on Light Water Reactor Severe Accident Evaluation</u>, Cambridge, MA, Aug. 28-Sept. 1, 1983 (American Nuclear Society, LaGrange Park, IL, 1983), p. TS-4.1-1.

10. D. J. Osetek et al., in: <u>Proc. Top. Mtg. Fission Product Behavior and Source Term Research</u>, Snowbird, UT, 1983 (American Nuclear Society, LaGrange Park, IL, 1984), p. 22-1.

11. R. Hargreaves and D. A. Collins, J. Br. Nucl. Energy Soc. <u>15</u> (1976) 311.

12. S. W. Tam, P. E. Blackburn, and C. E. Johnson, in: <u>Proc. Int. Mtg. Thermal Nuclear Reactor Safety</u>, Chicago, IL, Aug. 29-Sept. 2, 1982, pp. 101-110.

13. H. Kleykamp, J. Nucl. Mater. <u>131</u> (1985) 221.

14. P. Hofmann and J. Spino, J. Nucl. Mater. <u>127</u> (1985) 205.

15. American Nuclear Society, <u>Report of the Special Committee on Source Terms</u> (September 1984).

16. P. E. Blackburn and C. E. Johnson, <u>Light Water Reactor Fission Data Assessment</u>, ANL-82-42 (September 1982).

17. A. W. Cronenberg and D. J. Osetek, accepted for publication J. Nucl. Mater. (1987).

18. A. W. Cronenberg and D. J. Osetek, in: <u>Am. Chem. Soc. Severe Accident Chemistry Symp.</u>, Anaheim, CA, Sept. 8-12, 1986.

19. G. W. Parker and C. J. Barton, in: The Technology of Nuclear Reactor Safety, Vol. 2, eds. T. J. Thompson and J. G. Beckerley (MIT Press, Cambridge, MA, 1983), pp. 574-584.

20. D. J. Osetek, J. K. Hartwell, and A. W. Cronenberg, Presented at: Int. ANS/ENS Topical Mtg. on Thermal Reactor Safety, San Diego, CA, Feb. 1986.

21. C. M. Allison, E. R. Carlson, and R. H. Smith, in: Proc. Int. Mtg. on Light Water Reactor Severe Accident Evaluation, Cambridge, MA, Aug. 28-Sept. 7, 1983 (American Nuclear Society, LaGrange Park, IL, 1983).

22. R. V. Strain, in: Proc. Top. Mtg. Fission Product Behavior and Source Term Research, Snowbird, UT, 1983 (American Nuclear Society, LaGrange Park, IL, 1984), p. 2.1.

23. R. V. Strain, Argonne National Laboratory, private communication (1985).

24. U. S. Nuclear Regulatory Commission, Technical Basis for Estimating Fission Product Behavior During LWR Accidents, NUREG-0772 (June 1981).